Research Paper / Groundwater

Can Karst Conduit Models be Calibrated? A Dual Approach Using Dye Tracing and Temperature

Corresponding author:
James L. Berglund, Department of Earth and Environmental Science, Temple University, Philadelphia, PA, USA, 19122, james.berglund@temple.edu,
now at Montana Bureau of Mines and Geology, Montana Tech, Butte, MT, USA, 59701, jberglund@mtech.edu

Laura Toran
Department of Earth and Environmental Science, Temple University, Philadelphia, PA, USA, 19122, ltoran@temple.edu

Ellen K. Herman
Department of Geology, Bucknell University, Lewisburg, PA, USA 17837, ekh008@bucknell.edu

Key words: karst modeling; spring; FEFLOW; conduit flow; dye trace; temperature

CITATION:
Berglund, J.L., Toran, L., and Herman, E.K. 2020. Can Karst Conduit Models be Calibrated? A Dual Approach Using Dye Tracing and Temperature. *Groundwater*, Accepted.

Abstract
Modeling flow and transport using both temperature and dye tracing provides constraints that can improve understanding of karst networks. A laminar flow and transport model using the Finite Element Subsurface Flow Model (FEFLOW) simulated the conduit connection between a sinking stream and spring in central Pennsylvania to evaluate how conduit morphology might affect dye transport. Single and overly tortuous conduit models resulted in high concentrations as dye flowed back into the conduit from the matrix after dye injections ceased. A forked conduit model diverted flow from the main conduit, reducing falling limb dye concentration. Latin Hypercube Sampling was performed to evaluate the sensitivity of 52 parameter combinations (conduit hydraulic conductivity, conduit cross-sectional area, matrix transmissivity, matrix porosity, and dispersivity) for 4 conduit geometry scenarios. Sensitivity of arrival time for 50% of the dye indicated no parameter combinations which simulate falling limb dye concentrations for tortuous geometries, confirming the importance of the forked geometry regardless of other parameters.

Temperature data from high-resolution loggers were then incorporated into the forked conduit model to reproduce seasonal spring temperature using variable sink inflow. Unlike the dye trace models, the thermal models were sensitive to other model parameters, such as conduit cross-sectional area and matrix transmissivity. These results showed this dual approach (dye and temperature) to karst network modeling is useful for 1) exploring the role of conduit and matrix interaction for contaminant storage, 2) constraining karst conduit geometries, which are often poorly understood, and 3) quantifying the effect of seasonal trends on karst aquifers.

Introduction
Background
Although the conceptual model of a karst aquifer consisting of conduits embedded in a fissured rock matrix has been recognized since the 1960s (White, 1969), our understanding of the interactions between the conduit and matrix is still limited. Water in the matrix and conduits has different residence times and thus different geochemical signatures; these different residence times have implications for solute transport and risk assessment in karst aquifers. The conduits transport contaminants rapidly, while the matrix provides slow release of contaminants. Geochemical signatures have provided evidence for return of matrix water to conduits (Frank et al., 2019; Bailly-Comte et al., 2011; Martin and Dean, 2001). These studies used SO_4, conductivity, and Na-Cl to estimate matrix contributions, in particular during high flows. Additional indicators of conduit-matrix interaction include thermal response (Covington et al., 2011), numerical models of solute transport (Ronayne, 2013) and hydrographs (Bailly-Comte et al., 2010), spring discharge recession (Fiorillo, 2014; Chen and Goldscheider, 2014), and Mg/Ca ratio variation during storms (Toran and Reisch, 2013).

Temperature has been used as a natural tracer to better characterize karst recharge, flow, and conduit geometry. Birk et al. (2006) modeled storm response in a hypothetical karst conduit with temperature as a tracer to show interaction with the surrounding bedrock matrix dampened the temperature signal. Later models incorporated tracer test field data to evaluate these relationships (Luhmann et al., 2015, 2012) and included varying geometries to compare dampening effects (Covington et al., 2011; Covington and Perne, 2015). Annual temperature data were used to classify springs based on their seasonal and short-term temperature variations (Luhmann et al.,

2011). The vulnerability of karst flow systems to changing climate conditions has also been explored due to the sensitivity of karst systems to varying recharge and temperature (Hartmann et al., 2014a; Hartmann et al., 2014b; Li et al., 2016). For one hypothetical karst system, variations in groundwater temperature were seen to be a function of both the intensity and the seasonal timing of storm events (Brookfield et al., 2017).

Models must account for the dual-porosity (conduit and matrix) system (Taylor and Greene, 2008) in order to predict where the mass is stored and how it is being transported. For example, Birk et al. (2006) found that modeling transport without interaction with the matrix can lead to a 50% over-estimation of conduit size. Variable geometry with matrix interaction requires the use of specialized flow and mass transport model codes which can handle conduits, such as FEFLOW (Diersch, 2013) and MODFLOW-CFP (Shoemaker et al., 2008). Other modeling approaches involve compartments for dual porosity (Hartmann et al., 2017; Xu et al., 2018) and equivalent porous media models with mobile and immobile zones (Field and Pinsky, 2000; Birk et al., 2005). However, if the karst geometry network can be approximated, it provides a more realistic approach.

The geometry of karst networks has been studied through cave mapping, modeling, and dye tracing. Palmer (1991) distinguished branching, mazework, and spongework caves based on gradients and point versus diffuse recharge. Both epigenic and hypogenic caves are linked to mazework patterns (Palmer 2011). Dreybrodt (1996) and Siemers and Dreybrodt (1998) developed models of early karst development that showed widening occurs after the outlet is connected to the inlet and that short passages are favored. Kaufmann and Braun (1999, 2000) also found short passages were preferred especially in systems with a point sink rather than diffuse recharge. This finding held even for conduits within a permeable matrix. Filipponi et al. (2009) examined 18 large caves and examined statistical patterns of passage orientation and relation to bedding plains. They found caves were focused in a relatively small percentage of bedding planes. There are numerous investigations of karst networks through dye tracing. Two examples which link tracer breakthrough to conduit geometry are Goldscheider (2005) and Lauber et al. (2014). Goldscheider conducted 16 dye tracer tests in a complexly folded system with karst conduits. Long tails were associated with matrix diffusion in particular as heads in the conduit declined after a storm event. Lauber et al. (2014) were able to inject dye both into a sink and into the cave to distinguish flow paths in the vadose zone and saturated zone. The cave injection also identified greater dispersion in a wider cave; however, access to conduits for dye injection is not typical.

Stochastic models can also be used to estimate karst geometry. Ronayne (2013) found that conduit-matrix exchange reduced the influence of conduit flow paths using multiple realizations of karst networks with differing tortuosity. Borghi et al. (2012) generated random karst networks based on both geology and hydrology. They found strong connectivity led to short paths to the outlet with simpler path geometry and produced branching networks by overlaying multiple convergent networks. Similarly, Borghi et al (2016) found that only a small number (about 1%) of randomly generated networks produced results that matched their synthetic tracer test. It was easier to find fits to simplified geometries. Despite these findings there are still uncertainties regarding effects of conduit geometry and matrix interactions on flow and transport in karst. The difficulty in predicting conduit geometries leads to uncertainties in predicting the effects of

heterogeneity (Geyer et al., 2013), developing transit time predictions (Ghasemizadeh et al., 2016), and determining appropriate scales of modeling (Hartmann, 2016).
Thus, our inability to accurately take into account the geometry of conduits is still a fundamental limitation to developing accurate models. The research presented here examined whether conduit geometry can be a calibration parameter by comparing specific features of conduit networks: tortuosity and branching. Calibration was tested through use of two tracers, dye and temperature, to model a sinking stream and spring rise system. This dual tracer approach was further used to evaluate parameter sensitivity for each tracer.

Study Site

The study site (Figure 1) includes a sinking stream and a spring located in the folded carbonate bedrock of central Pennsylvania's Valley and Ridge Province (Berg et al., 1980). The stream flows into a sinkhole (Tippery Sink) which has been previously traced to the spring (Tippery Spring) 750 meters to the southeast (Hull, 1980). The adjacent Near Tippery spring is not connected to the sink, also based on the dye tracing, with other nearby springs and seeps which have not been monitored. The perennial stream flowing into Tippery Sink is sourced from the upland siliciclastic bedrock ridgetops. Rare earth element and Ca/Zr ratio analysis showed spring discharge is strongly connected to the inflow at Tippery Sink (Berglund et al., 2019). This strong connection between the sink and spring is further evident in the temporal variation in water temperature at Tippery Spring, with annual temperature variations monitored and described as part of the Shuster and White (1971) study, and short-term event-scale temperature variations further described by Toran et al. (2018).

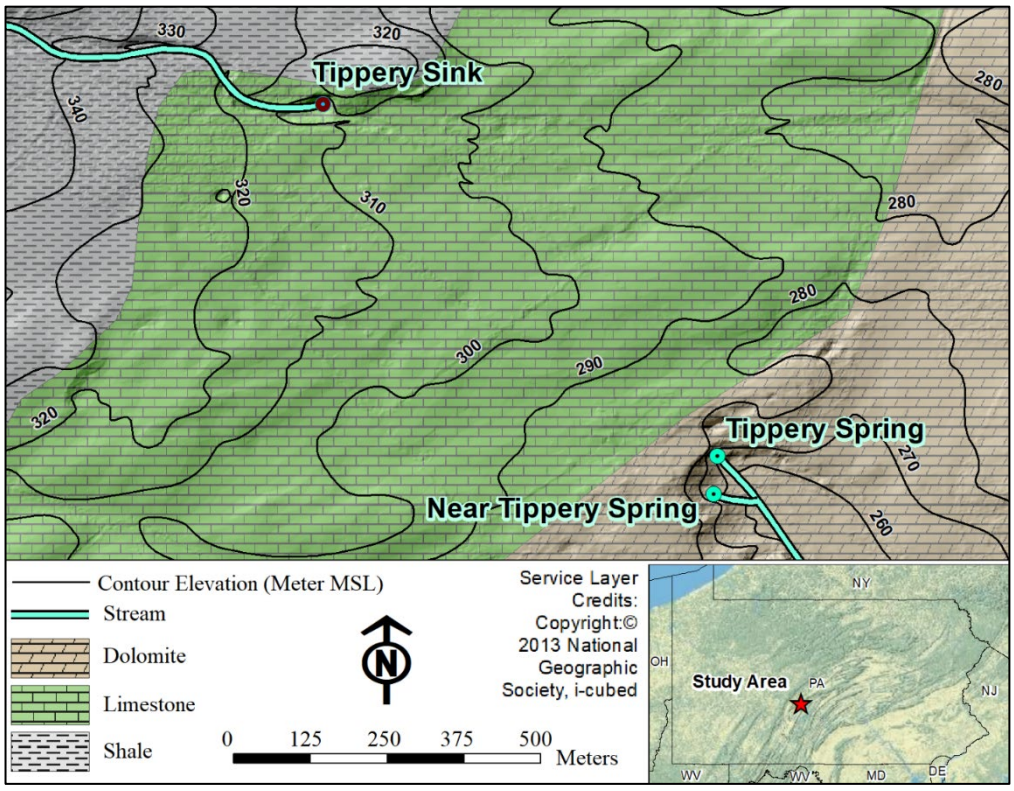

Figure 1. Locations of Tippery Sink, Tippery Spring, and Near Tippery Spring. Elevation contours in meters MSL.

Methods

Quantitative Dye Tracing

A dye trace using a controlled injection with continuous monitoring was performed to more precisely characterize the connectivity between the sink and the spring, following methods similar to Gouzie et al. (2015). Fluorescein sodium salt (CAS #518-47-8) was mixed with stream water to form a liquid dye with a concentration of 12 g/liter and injected into the sinking stream at a rate of 61 (+/- 1) mL/minute for 9 hours, for a total injection volume of 32.9 liters and a total dye mass of 357 grams. The drip point was 15 meters upstream of where the stream sinks in order to ensure mixing (Supporting Information, Figure S1). Sinking stream discharge was 14 L/s throughout the test. A Cyclops-7 Submersible logger measured fluorescein dye concentrations at the spring at a sample interval of 1 minute from May 25-29, 2018. The instrument was calibrated in the lab to provide output concentrations in µg/L. The dye flux plot for the sink and spring showed a 65% recovery, with a 36-hour lag between injection start and peak recovery (Figure 2). These data were used as input and calibration for the model.

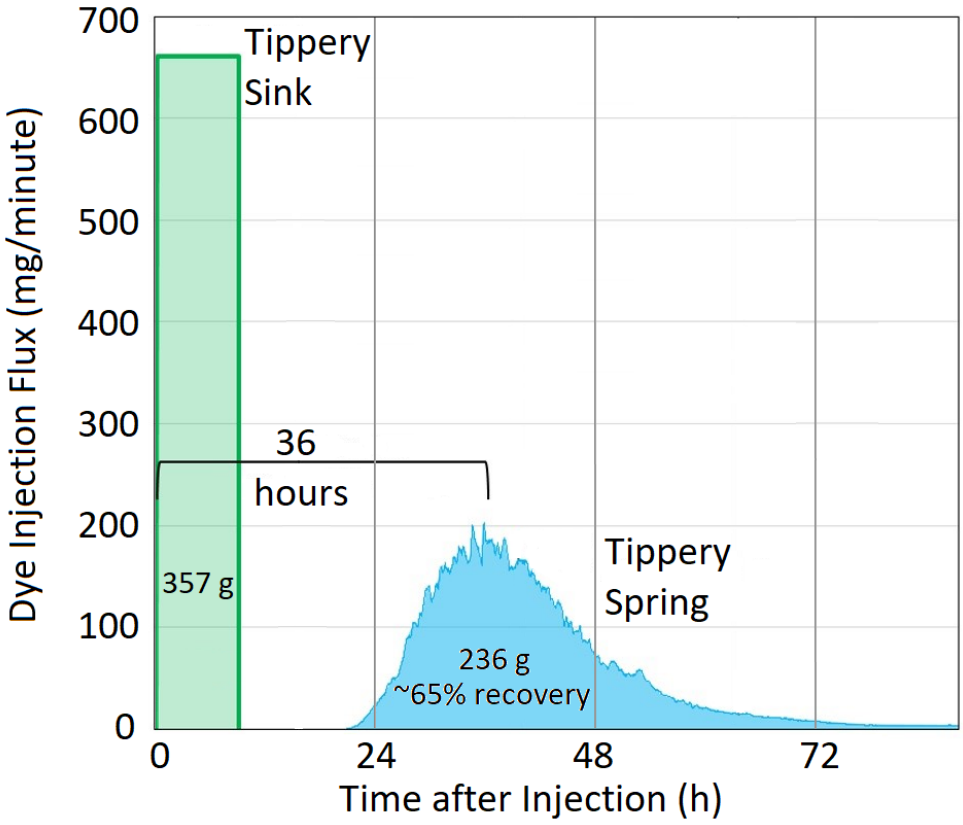

Figure 2. Dye trace results. The dye flux in at Tippery Sink (green) was used as a model input, while the dye flux out at Tippery Spring (blue) was a model target.

Continuous Temperature Monitoring of Sink and Spring

Loggers were used to measure sink and spring temperature, along with spring water level. An Onset Tidbit logger measured water temperature at the sink at a 15-minute interval. An Onset HOBO logger installed at the spring measured water temperature and pressure at 15-minute interval. Water pressure was converted to discharge for the spring using a weir installed near the spring mouth.

Logger data for temperatures at the sink and spring from April to early December 2017 was used as input and calibration (respectively) for the model presented here (Figure 3). Data from late December through March were not used as temperature in the sink often approached or fell below freezing due to a combination of lower air temperatures and low flow. For the modeled time period, the sink's water temperature varied from 6º Celsius in April to 22º C in July and down to 2º C by December, closely reflecting ambient air temperatures. The spring's water temperature also showed seasonal trends albeit buffered compared to the sink. In April, the spring's water temperature was around 7º C, rising to a high of 15º C in June, and falling to 10º C by December. While the sink showed a combination of diurnal variations and storm response in temperature, the spring's short-term variations were the result of storm events, as noted for the rainy season period from April to July. The lack of short-term variations from August to December reflected the dry season evident by declining spring discharge and fewer storm spikes.

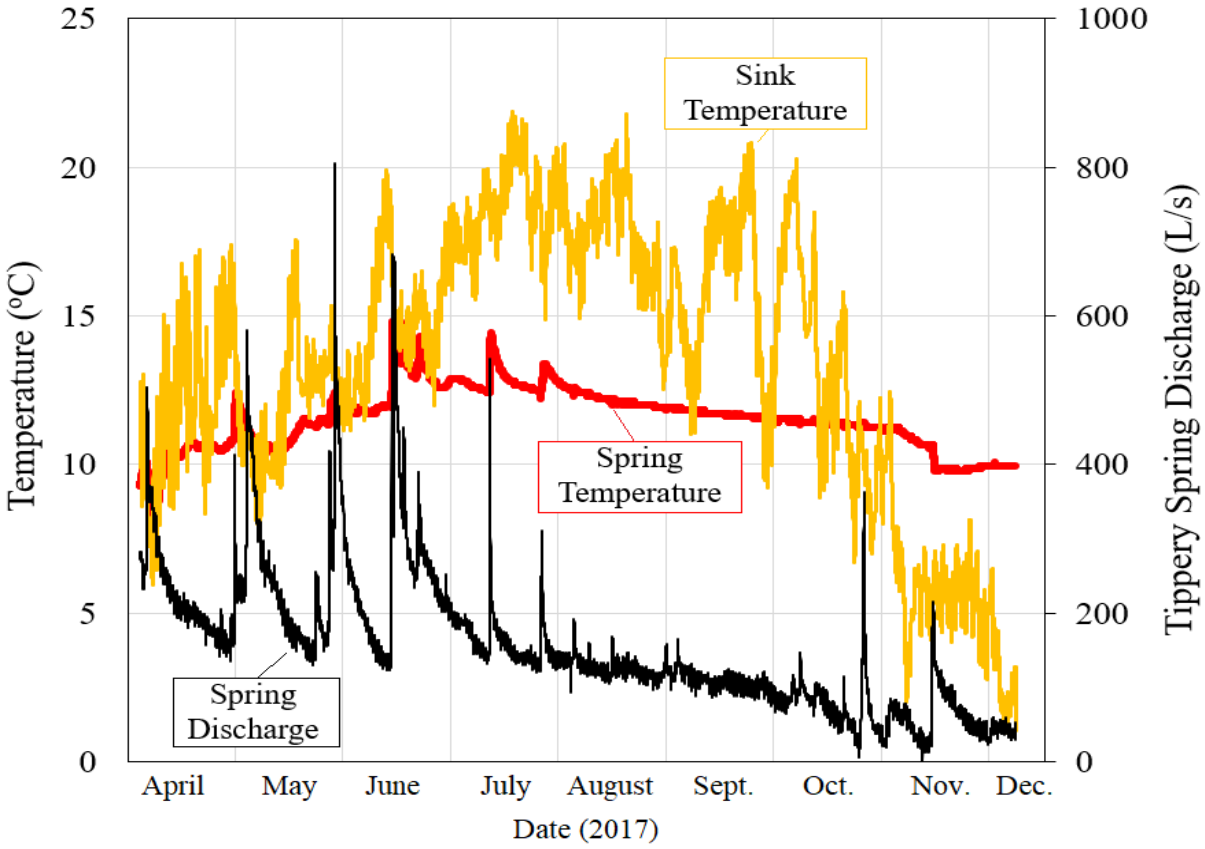

Figure 3. Temperature of Tippery Sink and Tippery Spring, and discharge for Tippery Spring, from April to December 2017.

Flow and Transport Modeling and Sensitivity Analysis

Solute and heat transport between the sink and spring were modeled using the finite element groundwater flow and transport modeling code FEFLOW (Diersch, 2013). The flow model was two-dimensional with laminar flow. Flow was steady state across the 4 days of the dye trace and included seasonal variation (but not daily or storm variation) for the 8-month period for seasonal

temperature variations. Although FEFLOW has been used successfully in karst studies of steady state and seasonal head distributions (Dafny et al., 2010; Kavouri and Karatzas, 2015), the application here focused on transient solute and heat transport modeling between a sinking stream and a spring to help constrain conduit geometry.

The two-dimensional domain for each FEFLOW model was 300 meters by 1000 meters wide with a conduit connecting a sink input and spring output spaced 750 meters apart (Supporting Information, Figure S2). The domain was refined into an irregular unstructured triangular grid with cell sizes ranging from coarse (20 meters) for the majority of the model to fine (1 meter) around the conduit. While runs with finer mesh around the conduit were conducted, they greatly increased run time with no appreciable change in the modeled dye breakthrough curve. The grid was oriented along the direction of the conduit. A one-dimensional flow field was set up in the matrix using specified head boundary conditions at either end of the model estimated from elevation contours for both the sink and spring based on USGS topographic maps. No-flow boundaries were used perpendicular to the specified head boundary. The flow field in the conduit was modeled as specified discharge boundary condition nodes, with inflow values based on occasional field observations for the sink and discharge values from a pressure transducer and weir at the spring. A recharge value of 1 m/year was used throughout the matrix, exclusive of the area affecting the conduit to represent focused recharge. As the head values in the model largely controlled by the sink inflow value and the upgradient constant head boundary, reducing the recharge value by half and one third had little overall effect on the model results (see Supporting Information, Figure S13).

The conduit connecting the sink and spring and surrounding porous media matrix were modeled as a combined flow system as described by Diersch (2013). Governing equations for flow, mass transport, and heat transport for the porous media matrix are provided in the Supporting Information. The governing equation for flow incorporates parameters for specific storage, hydraulic conductivity, viscosity, and hydraulic head, while the equations for mass and heat transport incorporate additional parameters such as porosity, solute concentration, fluid/solute/heat flux, molecular diffusion, mass transfer coefficients, temperature, and thermal dispersion. The thermal equations require thermal conductivity of fluids and solids, and specific heat capacity. These equations are further adapted to include the discrete conduit, which is modeled as a 1-dimensional feature interconnected to the surrounding aquifer. The conduit is modeled with laminar, saturated Darcy flow (Diersch, 2013). Turbulent flow is often incorporated within a dispersion term, and dispersion was varied in the model. Modeled conduits had varying tortuosity (τ) values, with tortuosity equal to the length of the conduit between the sink and spring divided by the straight-line distance between the sink and spring, with a straight conduit having $\tau = 1$. Governing equations for flow, mass transport, and heat transport include an additional parameter for conduit radius, along with separate values for parameters such as hydraulic conductivity, molecular diffusion, mechanical dispersion, and solute retardation in the conduit. Communication between the conduit and surrounding matrix is determined from a transfer coefficient which is dependent on the size of the conduit and porosity along with other parameters for mass flow, such as solute retardation and chemical decay, and parameters for heat flow, such as the density and specific heat capacity of water (see Supporting Information). Four base conduit geometry templates were used throughout the models; Geometry 1, a single straight conduit ($\tau = 1$); Geometry 2, a straight, forked conduit ($\tau = 1$); Geometry 3; a single

tortuous conduit (τ = 1.1), and Geometry 4, a mixed anastomosing conduit pair (τ = 1.0 and 1.15). Model scenarios with varying discharge or slight variations in their conduit geometry are labeled with their respective geometry number followed by a letter; e.g. Models 1A and 1B both use the single straight conduit of Geometry 1, but have different sink flow values (Table 1). These geometries were selected to be representative of features which are typical in karst (Palmer, 1999), but with a simplified geometry that reflects the importance of the most direct, connected flow path (Siemers and Dreybrodt, 1998). For example, the forked geometry might represent a mazework or overlapping convergent system where only the passages with a direct connection between the inlet and an outlet are included. Network simplification is described in Borghi et al. (2012, 2016) as a function of karst flow paths rather than actual cave geometry. Focused recharge (rather than dispersed) can lead to a system that has branches distributing flow (Borghi et al., 2012; Palmer, 1999). As mentioned previously, multiple springs occur in the area which indicate a distributed system, but they have not all been monitored. The terminations of the distributary conduits in the forked conduit model (geometry 2) were modeled as these potential springs with similar discharge. These models were used to narrow the initial base model parameters to be tested for sensitivity analysis and to determine the influence of varying conduit geometry.

Table 1. Summary of Model IDs, Geometries, and Description.

Model ID	Conduit Geometry ID	Description
1A	1	Straight conduit, full sink flow
1B	1	Straight conduit, low sink flow
1C	1	Straight conduit, variable sink flow
2A	2	Forked conduit, full sink flow
2B	2*	Forked conduit, medial branch
2C	2*	Forked conduit, proximal branch
2D	2	Forked conduit, variable sink flow
3	3	Tortuous conduit, low sink flow
4	4	Anastomosing conduit, low sink flow

*Modified

A Latin Hypercube (LHC) sensitivity analysis (Mckay et al., 1979) was conducted on the four conduit geometries to evaluate how parameters influence the results and whether a different conduit configuration could be fit by varying input parameters. This statistical method is often used to produce random parameters from a multidimensional distribution using as few total combinations as possible. This parsimony is accomplished by dividing parameters into discrete rows and columns in which parameter combination points occupy cells in which there is 1) only one point for each column/row combination cell, 2) each discrete row and column has an associated point, and 3) points do not share rows and columns with other points. LHC is multidimensional and can satisfy parameter diversity for *n* dimensions.

Five parameters were varied across typical ranges: conduit hydraulic conductivity, conduit cross-sectional area, matrix transmissivity (same as matrix hydraulic conductivity due to a constant 1-

meter thick aquifer thickness), matrix porosity, and a dispersivity modifier (multiplication factor applied to both longitudinal and transverse dispersivity) (Table 2). Longitudinal dispersivity was 13.3 times larger than transverse dispersivity for all model runs, which is within the typical range of ratios reported by Dassargues and Derouane (1998). A uniform distribution of parameter combinations was varied around the mean (base) parameter value, and the base values were typical for this formation and the scale of the study. The sensitivity analysis was applied to the dye trace model only, as the temperature model took much longer to run for the 8.5-month calibration period. A more limited range in parameters was applied in the temperature model to evaluate sensitivity to geometry, matrix hydraulic conductivity, conduit hydraulic conductivity, and conduit radius. For the LHC sensitivity analysis, mean parameters were used as the base case (Table 2) along with fixed default parameters in FEFLOW for the heat capacity (810 J/kg/K) and thermal conductivity of the rock matrix (2.15 W/mK). These thermal values are typical of carbonate rock (Waples and Waples, 2004; Çanakci et al., 2007). A total of 52 model parameter combinations were modeled based on the LHC generated variables, or 13 models per conduit geometry.

Table 2. Latin Hypercube parameter input ranges.

Parameter	Mean (base)	Minimum	Maximum
Conduit Conductivity (m/s)	0.105	0.009	0.242
Conduit Cross-Sectional Area (m^2)	0.5	0.02	1.06
Matrix Transmiss-ivity (m^2/s)	$5.0x10^{-4}$	$1.3x10^{-5}$	$1.1x10^{-3}$
Matrix Porosity (n)	0.1	0.01	0.25
Dispersivity Modifier	1	0.03	2.41
Conduit geometry (integer)	2 (forked)	1	4

Results

Dye Trace Models

Initially, three conduit network models were compared (Figure 4) using similar input parameters to achieve a peak timing match to observed dye breakthrough. These three models all had a conduit cross-sectional area of 0.5 m^2, a bedrock matrix transmissivity of 0.0005 m^2/second, matrix porosity of 0.1, a longitudinal dispersivity of 1 meter and transverse dispersivity of 0.075 meter. Model 1A consisted of a single 750 meter straight conduit connecting the sink and spring with the base sink inflow value observed during the dye trace (14 L/s) and a conduit conductivity of 0.16 m/s. Model 1B also consisted of a single straight conduit connecting the sink and spring with a sink inflow value of 1.4 L/s and a conduit conductivity of 0.18 m/s, both values adjusted to match the peak. Model 2A consisted of a straight conduit connecting the sink and spring with a sink inflow value of 14 L/s and a conduit conductivity of 0.105 m/s, but with the addition of a conduit fork 150 meters from the sink which diverts flow to two side conduits.

Despite matching the observed dye peak arrival time, Model 1A resulted in a peak dye concentration (71 µg/L) that was nearly twice what was observed at the spring (38 µg/L), with 10-30 µg/L higher concentrations in the recession limb (Figure 4). Model 1B was able to produce a better fit in terms of both timing and concentration of the dye peak (40 µg/L), but required a sink inflow value below what was observed in the field (reduced from 14 L/s to 1.4 L/s). Conduit conductivity was also increased slightly from Model 1A to Model 1B in order to

maintain the correct peak arrival time, although no other parameters were changed. Additionally, the falling limb of the Model 1B dye curve was notably higher than what was observed in the field, ranging from 2-10 µg/L higher than observed. The results of Model 1A and Model 1B suggest that the flow between the sink and spring cannot be accurately simulated as a single conduit as it either results in too much modeled dye or requires an erroneously lowered sink inflow value.

Model 2A addressed the issues from Model 1A and Model 1B through the incorporation of a forked branch conduit geometry. This forked conduit diverts both flow and dye away from the main conduit, allowing for the full sink inflow value to be used as an input while also resulting in a decreased overall dye concentration reaching the spring. As such, Model 2A resulted in the best overall fit between modeled and observed dye breakthrough curves, modeling within 2 µg/L of observed concentrations throughout the entire dye breakthrough curve (Figure 4).

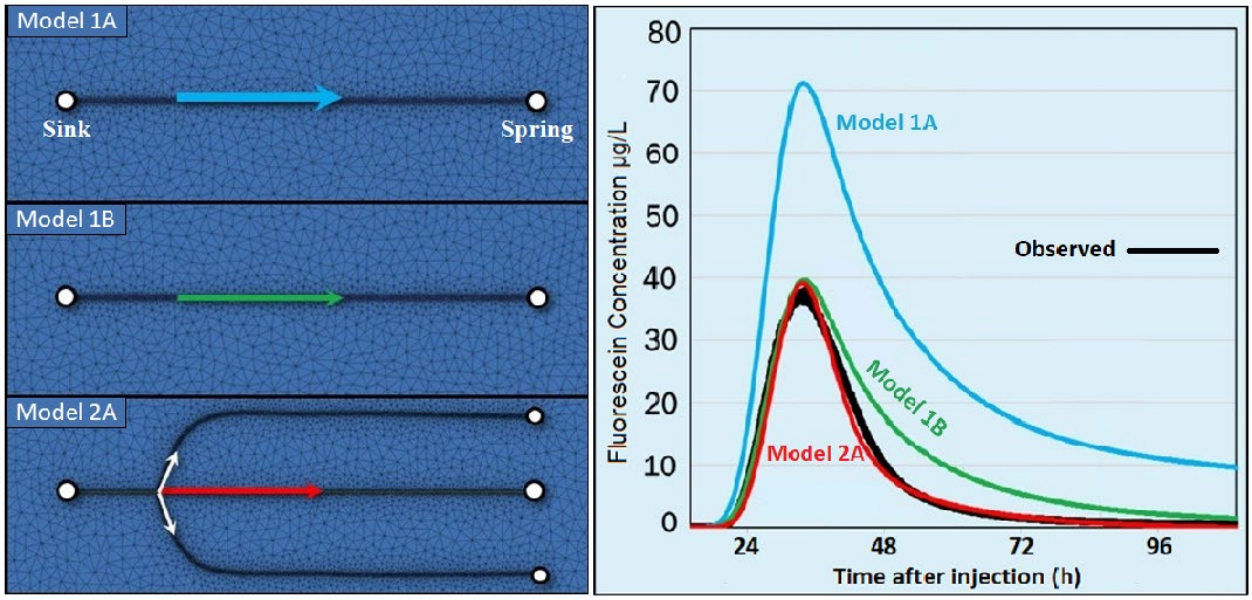

Figure 4. Initial dye trace models. Model 1A) full flow between sink and spring, Model 1B) reduced flow between sink and spring, and Model 2A) full flow into sink but diverted through forking branches between sink and spring. Dark black line indicates the observed fluorescein concentration at the spring.

The location of the conduit fork (as shown in Model 2A) also had an effect on both the timing and the peak concentration for a simulated dye breakthrough curve (Figure 5). For Model 2A (Distal Fork), the branch in the conduit was 600 m from the spring. Two other modeling scenarios were conducted with the same parameters in which the branch was moved closer to the spring; Model 2B (Medial Fork) and Model 2C (Proximal Fork). As the fork was moved closer to the spring and farther away from the sink for Model 2B and 2C, the simulated dye breakthrough curve arrived earlier (6.8 and 10.3 hours earlier, respectively) and also had progressively higher peak concentrations (60 and 71 µg/L, respectively, compared to the observed 39 µg/L). Decreasing the conduit conductivity for Model 2C (Proximal Fork) from 0.105 m/s to 0.067 m/s shifted peak arrival time to then match that of Model 2A (Distal Fork) (Figure S9), but the resulting dye concentration curve still did not produce as good a match as

Model 2A (Distal Fork). These results suggest that the location of flow branching can control the shape of the dye breakthrough curve, and that steady state high resolution dye trace studies may be useful to evaluate whether flow diversions occur and where the diversions might be located.

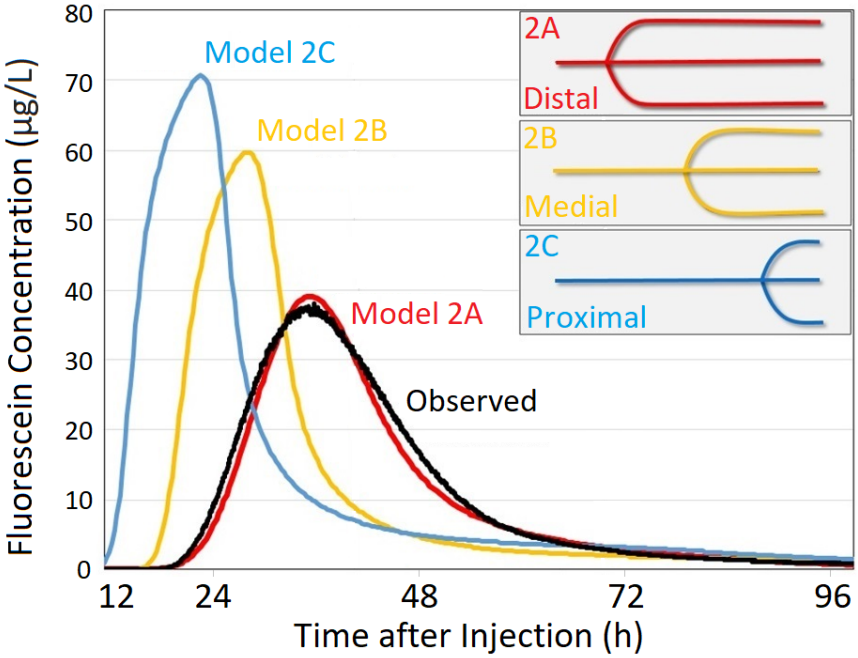

Figure 5. Varying dye peak responses based on location of conduit fork point between sink and spring.

Dye Trace Sensitivity Analysis Runs

Breakthrough curves from the LHC sensitivity analysis showed the effects of varying model parameters within each of the four conduit geometry scenarios (Figure 6). For a straight conduit (Geometry 1, Figure 6), 9 of the 13 modeled dye breakthrough curve concentrations were higher than the observed dye peak concentration, ranging from 50-170 µg/L compared to the observed 39 µg/L. For the forked conduit (Geometry 2, Figure 6) the modeled peak concentrations varied from higher (5 of 13, ranging from 60-115 µg/L) to lower (8 of 13, ranging from 2-35 µg/L) than observed, while having an equal number of scenarios with sooner and later peak arrival than observed. For the tortuous conduit (Geometry 3, Figure 6) the modeled dye peak concentration and arrival times were most similar to the straight conduit, although there was a notable buffering effect as 11 of the 13 scenarios had delayed peak arrival times. The anastomosing conduit system (Geometry 4, Figure 6) exhibited the greatest buffering effect as all of the scenarios had peak arrival times greater than observed and 10 of the 13 scenarios had peak concentrations below observed.

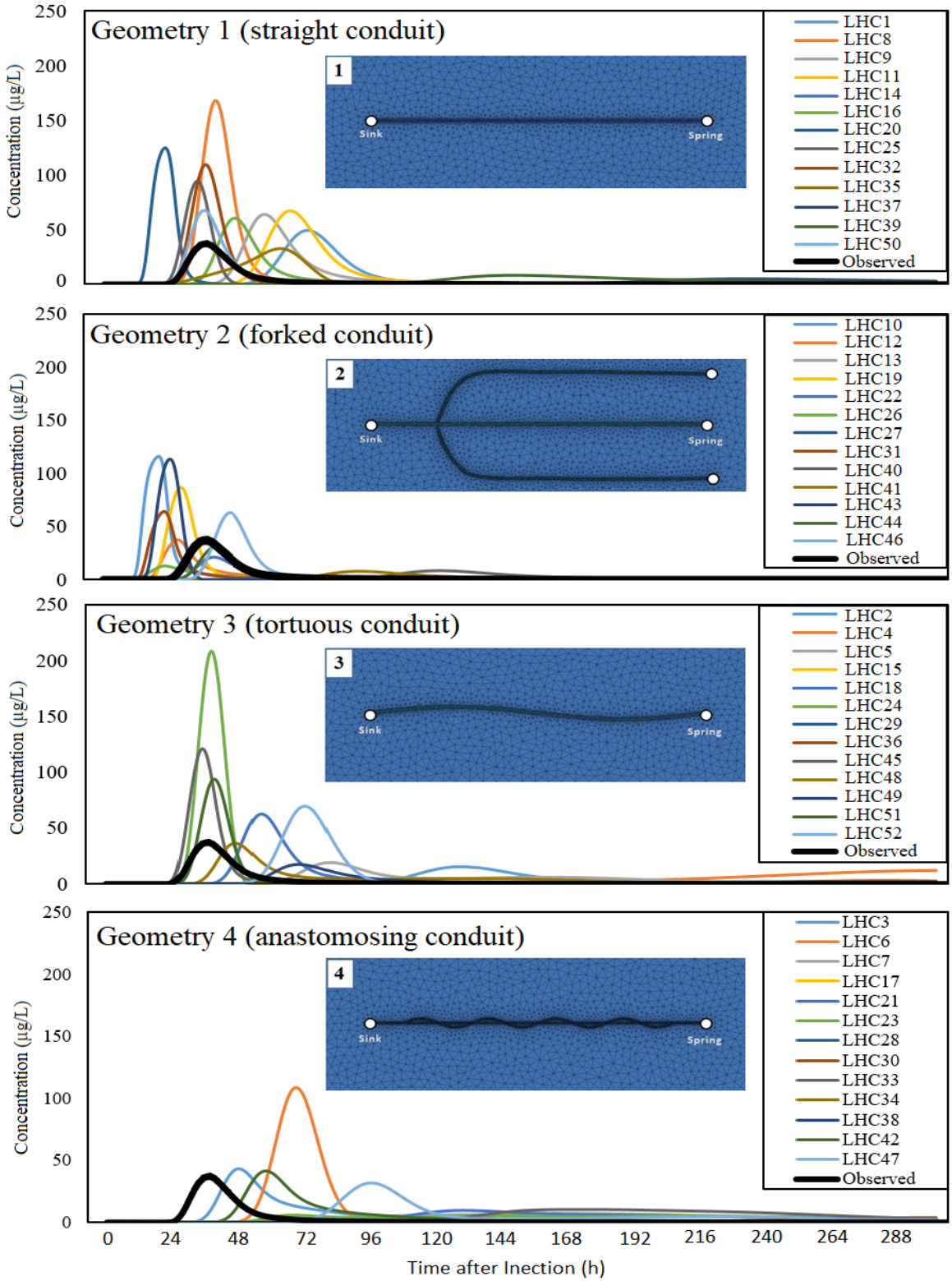

Figure 6. Latin Hypercube (LHC) dye trace model breakthrough curves for Geometry 1 (straight conduit), Geometry 2 (forked conduit), Geometry 3 (tortuous conduit), and Geometry 4 (anastomosing conduit). Some runs did not produce an observable breakthrough within the modeled time period. See Supplemental Information Table S1 for model run parameters.

Cumulative concentration and normalized cumulative concentration curves were used to distinguish dye breakthrough curve responses (Supporting Information, Table S1, Figures S3-S6). Diagnostic analyses included the time for 50% dye arrival, timing of dye peak arrival, width of the dye curve (calculated as the time difference from 16% arrival to 84% arrival), and the ratio between the modeled dye peak and observed and base model peak. Of the 52 models produced, 43 resulted in distinct dye curve peaks, while only 36 models showed a complete recovery within 12 days (total model run time, beyond the observed dye tracer recovery). The inability for some models to match the peak timing or even result in a dye breakthrough curve was largely the result of conduit conductivity, while lower conduit conductivity having the greatest non-geometry effect on dye recovery (Figure 7). This result only addresses timing, not peak height, which was influenced strongly by conduit geometry (i.e., the forked conduit).

The relationship between 50% dye arrival time and variable model parameters for each of the four conduit geometries showed that there were no parameter combinations which could make up for the increased spreading and longer travel times from the tortuous and anastomosing geometries (Figure 6). The best match to peak height and tail was seen for the forked conduit (Geometry 2). A decrease in conduit conductivity resulted in a greater amount of time for 50% of modeled dye to reach the spring (Figure 7) for three of the geometry scenarios (Geometries 1-3). For the anastomosing conduit (Geometry 4), the relationship between conduit conductivity and travel time was not apparent.

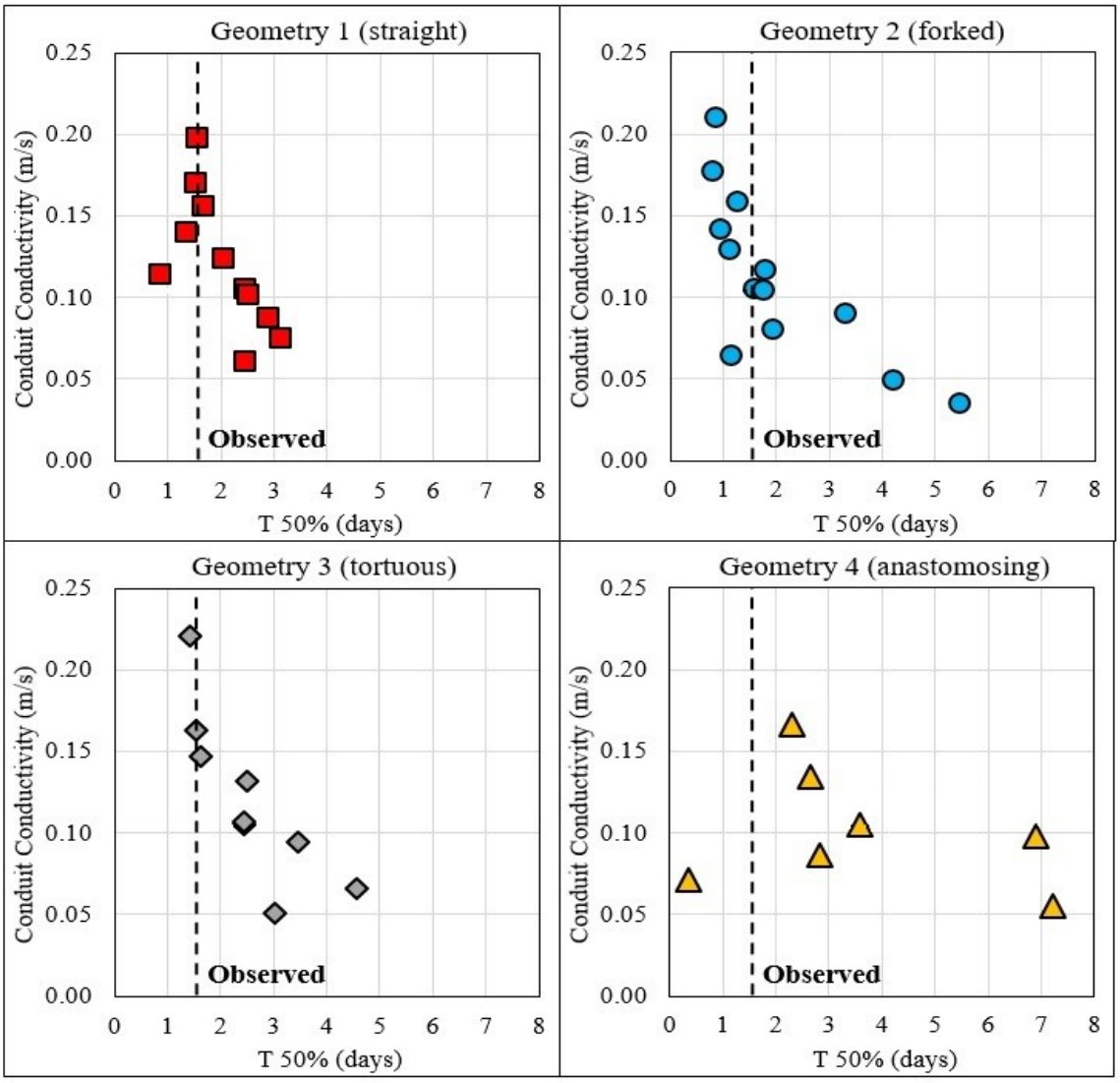

Figure 7. Modeled 50% dye arrival time vs. conduit conductivity for Conduit Geometry 1-4 scenarios.

Matrix transmissivity showed a weak positive relationship, with increased matrix transmissivity resulting in a longer 50% dye arrival time only for the forked geometry (Figure 8). Conduit cross-sectional area, matrix porosity, and dispersivity did not notably affect travel time (Supporting Information, Figures S7 to S9). Several additional geometries (semi-forked, varied conductivity of fork, reverse fork to represent a convergent network) were examined and included in the Supporting Information (Figures S10 to S12), but did not produce good matches to the tail of the breakthrough curve.

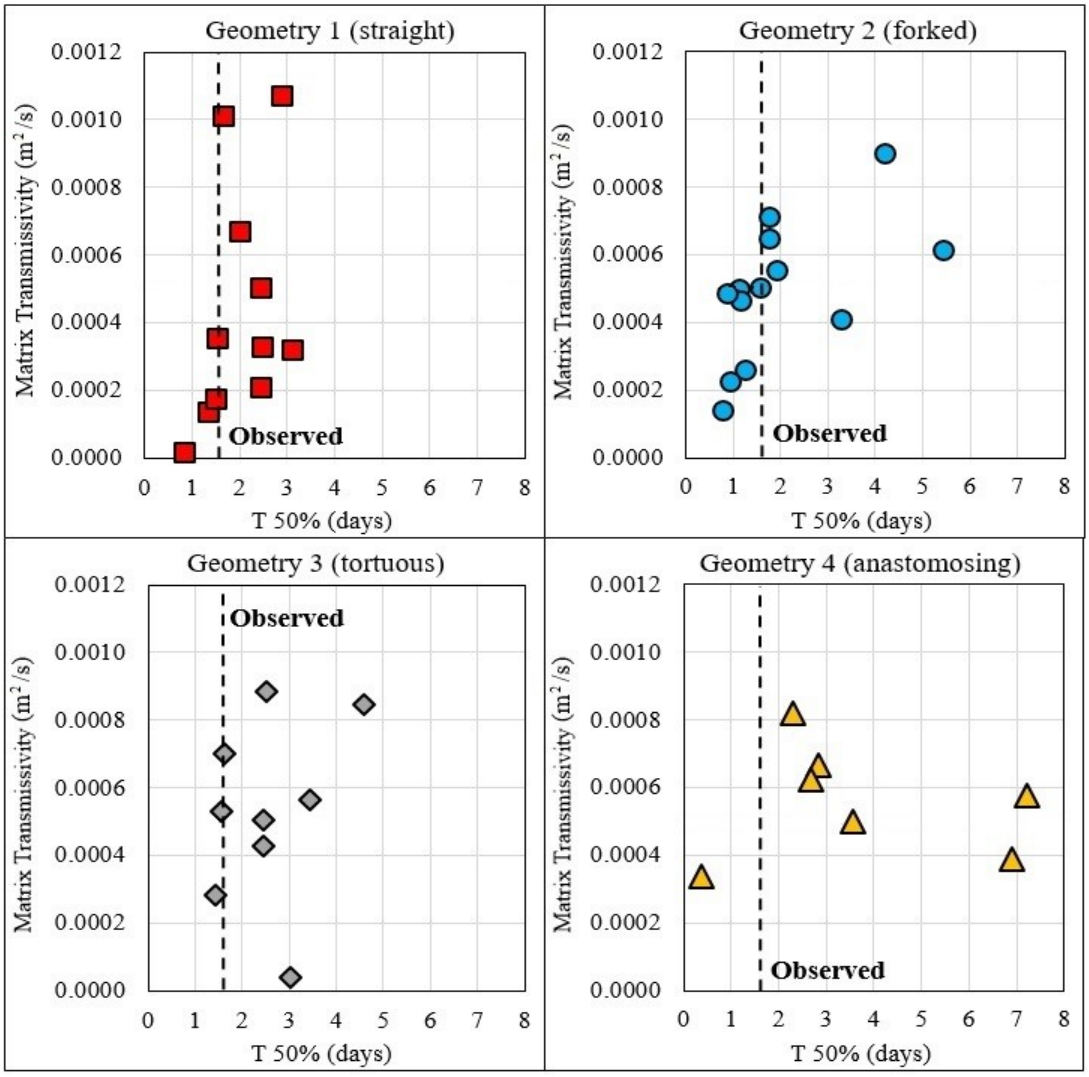

Figure 8. Modeled 50% dye arrival time vs. matrix transmissivity for Conduit Geometry 1-4 scenarios.

Temperature Models

A temperature model set up using the straight and forked geometries with constant sink inflow showed contrasts in seasonal responses (Figure 9a). Model 1A resulted in spring temperatures which were lower than observed from April to July and higher than observed from July to December. Models 1B and 2A produced spring temperatures that were 1-5° C below observed spring temperatures from April to August, while more closely matching (<1° C) observed spring temperature from August to December. Applying variable sink inflow rates provided an improved fit to observed seasonal temperatures for both straight and forked geometries (Figure 9b). These flow values were 60 liter/second from April to June, 30 liter/second from June to August, and 14 liter/second from August to December. The values selected were similar to observed values during periodic site visits and variation in discharge and number of storm events observed in the spring hydrograph (Figure 3). The flow value of 60 liter/second for the entire span from April to June may represent an average of storm and non-storm conditions, as some field visits during this time period showed lower sink flow (such as during the dye trace). The

sink likely has faster flow recession after storms than the spring, and a 14 liter/second value during the dye trace may be reasonable for the short duration dye trace (several days) in which rain had not occurred recently, despite the higher spring discharge. The details of discharge rate variation require further investigation, but these values resulted in a model which closely mimic observed spring temperature within 1 degree Celsius.

Both straight and forked conduits could produce seasonal temperature variations when the sink input discharge was varied seasonally. In addition, the forked geometry model showed an improved match to spring temperature data during storms, based just on seasonal temperature variation at the sink, but not including discharge variation during storms. Incorporating storm-scale variation in sink discharge would likely further improve agreement, but such transient inputs would increase run times significantly. This storm response further supported a forked geometry for the conduit.

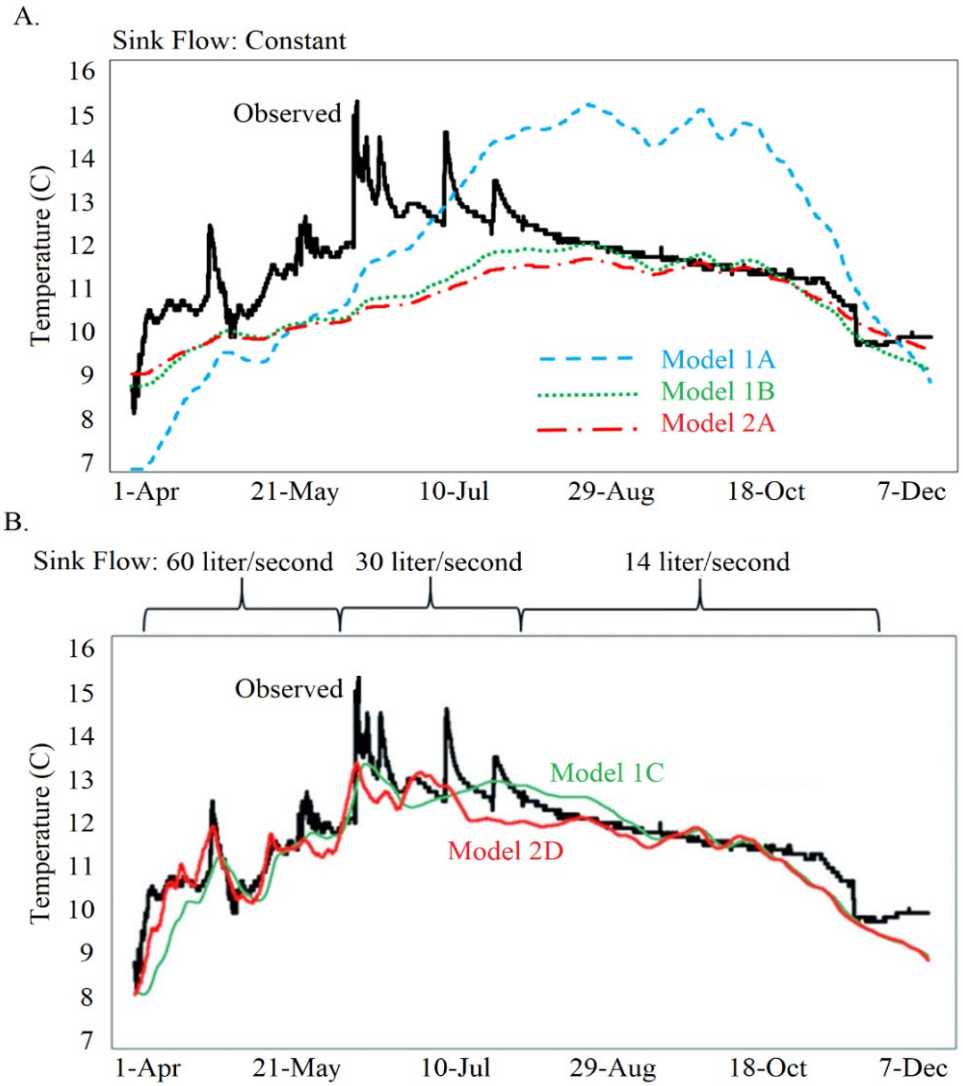

Figure 9. Modeled vs. observed spring temperature results using a steady sink inflow value for Model 1A, Model 1B and Model 2A. Temperature model results from the straight conduit geometry model and the forked conduit geometry model using variable sink inflow.

Temperature Model Sensitivity to Model Parameters

Spring temperature from April 8-29, 2017 was used to test the sensitivity of the temperature model to parameters by varying conduit conductivity, conduit diameter, and matrix transmissivity showed the most variation (Figure 10). These runs were conducted with the distal fork conduit (Geometry 2) as it had the best match to the dye trace results. As conduit conductivity increased, the resulting modeled spring temperature more closely mimicked sink temperature. Additionally, short-term diurnal temperature signals were better translated from the sink to the spring, resulting in more short-term variation in modeled spring temperature compared to the smoothed temperature signal resulting from a decreased conduit conductivity. A decrease in conduit conductivity resulted in both a lower modeled spring temperature and a buffered storm response.

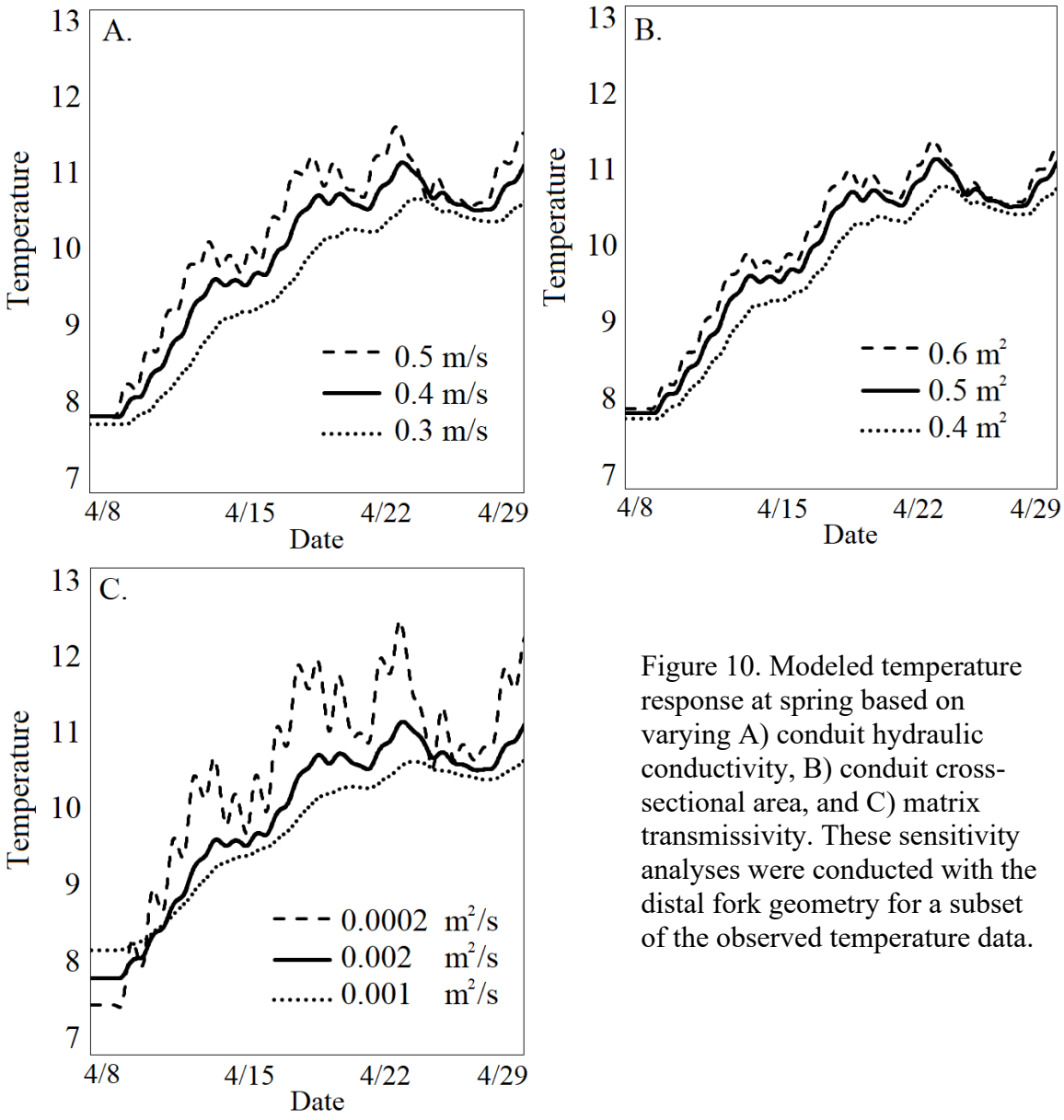

Figure 10. Modeled temperature response at spring based on varying A) conduit hydraulic conductivity, B) conduit cross-sectional area, and C) matrix transmissivity. These sensitivity analyses were conducted with the distal fork geometry for a subset of the observed temperature data.

Increasing conduit cross-sectional area results in less thermal equilibrium between the conduit water and surrounding rock due to a greater ratio between conduit area and circumference, reducing thermal interaction between the conduit and the surrounding matrix. In contrast, a reduction in conduit cross-sectional area results in more thermal buffering. Matrix transmissivity has the opposite effect, with an increased transmissivity creating more thermal buffering while a decreased transmissivity results in less thermal buffering.

Discussion and Conclusions

The modeling of dye injection and a natural tracer (temperature) at Tippery Spring illustrated how conduit geometry influences tracer breakthrough curves. The dye tracer provided data over the course of a day, while temperature signals included seasonal and storm variations to use in model fitting. Modeling with FEFLOW benefitted from the incorporation of discrete conduits, matrix interaction, and both mass and thermal transport.

Two important factors in model calibration were the influence of conduit geometry on conduit-matrix interaction and the sequential calibration to dye tracing and thermal response. Although there were a large number of model parameters, this sequential calibration resulted in greater model confidence by limiting possible range in conduit conductivity and geometry. By comparing simplified geometries, this modeling showed certain geometries were not realistic while others improved model fit.

Effect of Conduit Geometry and Matrix Interactions

The differences in peak dye concentration, dye falling limb concentration, and temperature buffering can be explained by conduit-matrix interactions in different geometries (Figure 11). An increase in tortuosity resulted in a decreased dye concentration peak and a more drawn-out dye recession limb. In this scenario the dye flowing into the matrix was only temporary as it then dispersed back into the conduit further down gradient, feeding the recession limb of the dye breakthrough curve. The temperature model with a tortuous conduit showed increased interaction with the bedrock matrix, creating a temperature dampening effect similar to the modeled dye trace in a tortuous conduit.

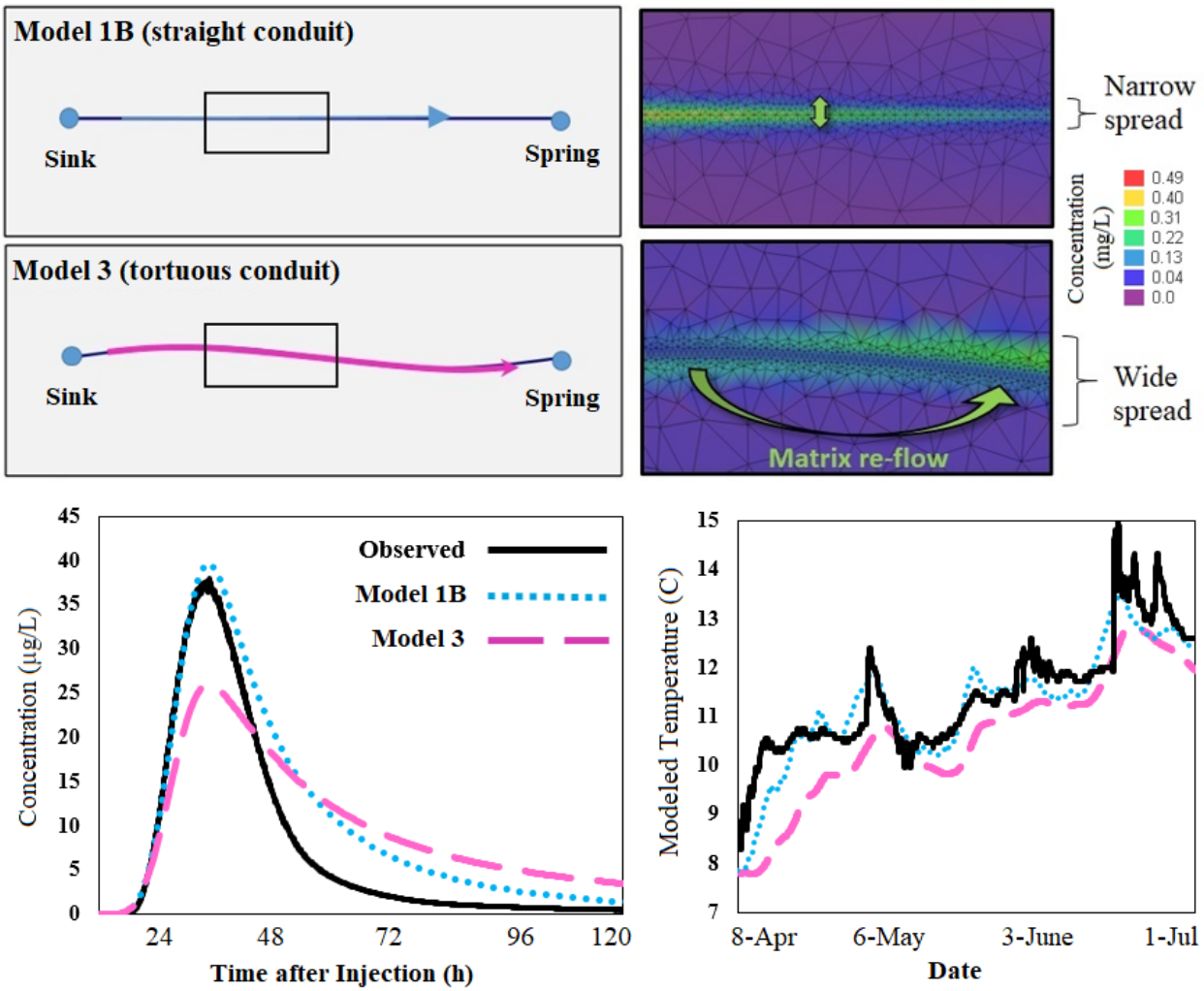

Figure 11. Effects of tortuosity on the falling limb of dye and temperature responses.

For a straight conduit (Geometry 1), the dye's longer recession and delayed temperature response were created by diffusion over time. Both the observed dye response and temperature better matched the sharper temperature peaks with a forked conduit (Geometry 2). Neither the LHC sensitivity analysis nor the variation in matrix parameters in temperature modeling were able to change the matrix-conduit interactions sufficiently to dampen this diffusion effect. Goldscheider (2005) observed similar diffusion from the matrix to the conduit in a series of dye tracer tests when head values changed due to storm events. However, our diffusion was modeled using steady state head scenarios rather than due to storm events.

Matrix parameters are important controls on conduit-matrix interaction, as low matrix transmissivity leads to less dye travel into the matrix and sharper dye peaks at the spring. Similarly, high conduit conductivity and cross section reduces dye travel into the matrix and leads to sharper peaks at the spring. The tortuous and anastomosing model scenarios showed the weakest sensitivity to matrix transmissivity and conduit conductivity and the fewest model runs matching either peak height or timing (Figures 6-8). Temperature modeling scenarios with weak matrix interaction showed overshoot on peaks and peak timing (Figure 10).

Differences in Model Sensitivity for the Two Models

Unlike the dye trace models, which were largely sensitive to just conduit conductivity and conduit geometry, the thermal models were sensitive to additional model parameters, such as conduit cross-sectional area and matrix transmissivity (Figure 12). Because the dye has less interaction with the matrix than temperature, its timing and concentration from sink to spring is largely a function of the travel time through the conduit. The temperature models are sensitive to more parameters because thermal properties of the matrix influence transport, so the initial determination of conduit conductivity and geometry from a dye trace reduces the number of valid solutions for subsequent temperature models. Dye trace models also have a much shorter model run time, which further makes them a useful first approach to conduit model setup.

This dual approach to karst model calibration using a temperature model set up from an initial dye trace resulted in greater model confidence by taking advantage of the sensitivity of each method. Both the dye and temperature models were sensitive to conduit geometry as it can have a noticeable effect on conduit-matrix exchange. Initially calibrating to matrix geometry using the dye trace limited the range in conduit conductivity and geometry for the temperature runs. Follow-on calibration to matrix transmissivity and conduit cross-sectional area helped limit the necessary combinations of parameters that need to be evaluated.

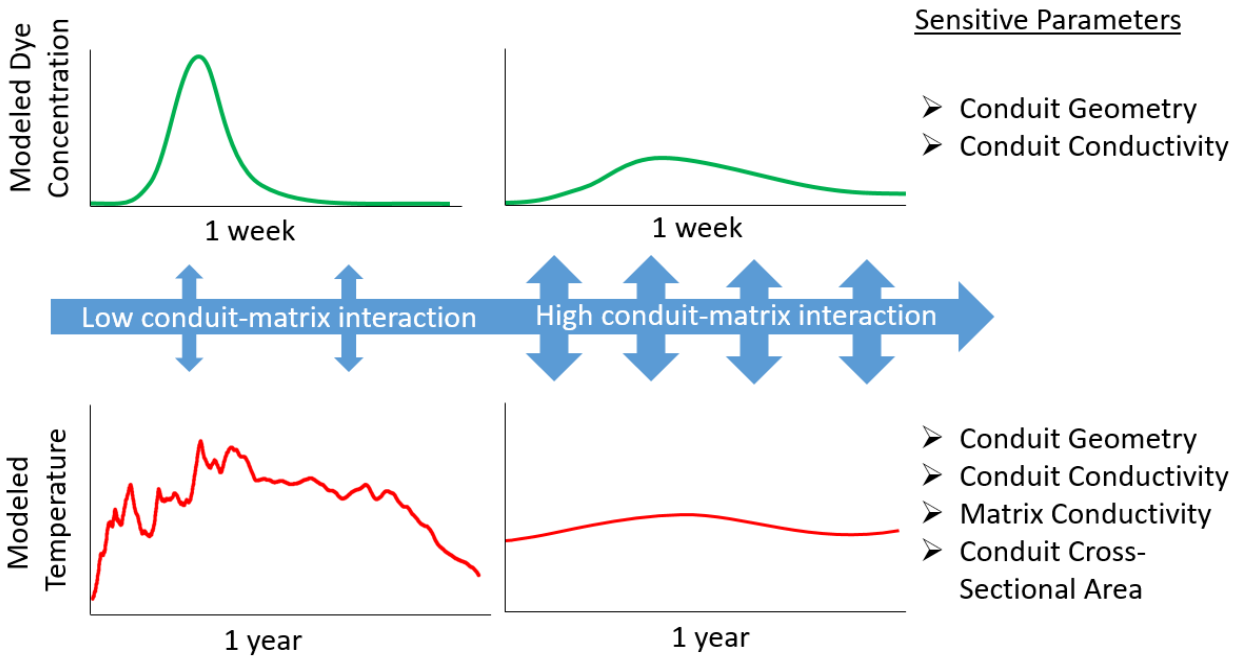

Figure 12. Conceptual summary diagram on the cause and effect of the degree of conduit-matrix interaction on temperature models and dye trace models. Within each section the dark bullets indicate resulting model behaviors while the open circles indicate model parameters which resulted in those behaviors.

Implications and Summary

The interaction between the conduit and the matrix is important for understanding storage of contaminants in karst systems. The dye and the temperature models each showed increased matrix interaction resulting from particular conduit geometries. Both a straight and a tortuous conduit network increased the degree of water-rock interaction, which would lead to more storage in the matrix and longer travel times from sink to spring. A decrease in water-rock interaction, as in the case of a forked conduit, allowed for more direct transmission to the spring resulting in higher peak concentrations. Although solute diffusion has been recognized as a secondary source in transport models, these results support using temperature as a tracer in karst to enhance conceptual understanding of conduit flow geometry and dynamics.

The dual approach presented here has the advantage of narrowing possible ranges of parameters and conduit geometries using the more field-intensive dye tracer in conjunction with seasonal variations and conduit-matrix interactions from high-resolution temperature monitoring. A suggested procedure for creating such a model includes: 1) beginning temperature logging at flow points using high-resolution, low-maintenance dataloggers, 2) performing the dye trace when steady-state conditions are met, 3) construct and test initial conduit models using results from the dye trace, and 4) incorporating the temperature data to extend model scenarios. While the dye trace was useful for setting up an initial model, obtaining the data is time-intensive and only represents a snapshot of flow from sink to spring. In contrast, water temperature is much easier to measure over long time periods, recording seasonal changes. However, in terms of model computation time, the short-term dye trace models ran in minutes, while the seasonal temperature model required hours to run. Thus, the variation in geometries, which is difficult to automate, was better suited to the dye tracer model. The advantages of using both dye and temperature to calibrate models are illustrative for other sites.

Acknowledgements

The authors would like to acknowledge the National Science Foundation's Hydrologic Sciences Program under award number 1417477. Special thanks to the landowners of the sink and springs who allowed us access. Additional thanks to DHI Group for the use of FEFLOW. Thank you also to the three reviewers for helping us improve our manuscript.

Supporting Information

Additional supporting information may be found at the end of this document that contains figures S1 through S12 and table S1 as referenced in the text above.

Please note "Supporting Information" is generally *not* peer reviewed. Wiley is not responsible for the content or functionality of any supporting information supplied by the authors. Any queries (other than missing materials) should be directed to the corresponding author.

References

Bailly-Comte, V., Martin, J.B., Jourde, H., Screaton, E.J., Pistre, S., Langston, A., 2010. Water exchange and pressure transfer between conduits and matrix and their influence on hydrodynamics of two karst aquifers with sinking streams. J. Hydrol. 386, 55–66. https://doi.org/10.1016/j.jhydrol.2010.03.005

Bailly-Comte, V., J.B. Martin, and E.J. Screaton, 2011. Time variant cross correlation to assess residence time of water and implication for hydraulics of a sink-rise karst system. Water

Resources Research, 47(5): W05547.
Berg, T.M., Edmunds, W.E., Geyer, A.R., 1980. Geologic Map of Pennsylvania (2nd ed.), Pennsylvania Geological Survey. Harrisburg, PA.
Berglund, J.L., Toran, L., Herman, E.K., 2019. Deducing flow path mixing by storm-induced bulk chemistry and REE variations in two karst springs: With trends like these who needs anomalies? J. Hydrol. 571. https://doi.org/10.1016/j.jhydrol.2019.01.050
Birk, S., Geyer, T., Liedl, R. M. Sauter, 2005. Process-based interpretation of tracer tests in carbonate aquifers. Groundwater, 43(3), pp. 381-388.
Birk, S., Liedl, R., Sauter, M., 2006. Karst spring responses examined by process-based modeling. Ground Water 44, 832–836. https://doi.org/10.1111/j.1745-6584.2006.00175.x
Borghi, A., Renard, P., Jenni, S., 2012. A pseudo-genetic stochastic model to generate karstic networks. Journal of Hydrology, 414, pp. 516-529.
Borghi, A., Renard, P., Cornaton, F., 2016. Can one identify karst conduit network geometry and properties from hydraulic and tracer test data? Advances in Water Resources, 90, pp. 99-115.
Brookfield, A.E., Macpherson, G.L., Covington, M.D., 2017. Effects of Changing Meteoric Precipitation Patterns on Groundwater Temperature in Karst Environments. Groundwater 55, 227–236. https://doi.org/10.1111/gwat.12456
Çanakci, H., Demirboğa, R., Karakoc, M.B. and Şirin, O., 2007. Thermal conductivity of limestone from Gaziantep (Turkey). *Building and environment*, *42*(4), pp.1777-1782.
Chen, Z., Goldscheider, N., 2014. Modeling spatially and temporally varied hydraulic behavior of a folded karst system with dominant conduit drainage at catchment scale, Hochifen-Gottesacker, Alps. Journal of Hydrology, 514, pp. 41-52.
Covington, M.D., Luhmann, A.J., Gabrovek, F., Saar, M.O., Wicks, C.M., 2011. Mechanisms of heat exchange between water and rock in karst conduits. Water Resour. Res. 47. https://doi.org/10.1029/2011WR010683
Covington, M.D., Perne, M., 2015. Consider a cylindrical cave: A physicist's view of cave and karst science. Acta Carsologica 44, 363–380. https://doi.org/10.3986/ac.v44i3.1925
Dafny, E., Burg, A., Gvirtzman, H., 2010. Effects of Karst and geological structure on groundwater flow: The case of Yarqon-Taninim Aquifer, Israel. J. Hydrol. 389, 260–275. https://doi.org/10.1016/j.jhydrol.2010.05.038
Dassargues, A., Derouane, J., 1998. A modelling approach as an intermediate step for the study of protection zones in karstified limestones. IAHS Publication Series of Proceedings and Reports, Intern Assoc Hydrological Sciences, 247, 71-80.
Diersch, H.-J.G., 2009. Discrete feature modeling of flow, mass and heat transport processes by using FEFLOW. White Papers, vol. 1, ch. 9. DHI-WASY, Berlin, Germany.
Diersch, H.-J.G., 2013. FEFLOW: a finite-element ground water flow and transport modeling tool. Springer Science & Business Media, Berlin, Germany.
Dreybrodt, W., 1996. Principles of early development of karst conduits under natural and man-made conditions revealed by mathematical analysis of numerical models. *Water Resources Research*, *32*(9), pp.2923-2935
Field, M.S., Pinsky, P.F., 2000. A two-region nonequilibrium model for solute transport in solution conduits in karstic aquifers. Journal of Contaminant Hydrology, 44(3-4), pp. 329-351.
Filipponi, M., Jeannin, P.Y. and Tacher, L., 2009. Evidence of inception horizons in karst conduit networks. *Geomorphology*, *106*(1-2), pp.86-99.

Fiorillo, F., 2014. The Recession of Spring Hydrographs, Focused on Karst Aquifers. Water Resour. Manag. 28, 1781–1805. https://doi.org/10.1007/s11269-014-0597-z

Frank, S., Geoppert, N., Ohmer, M., Goldscheider, N., 2019. Sulfate variations as a natural tracer for conduit-matric interaction in a complex karst aquifer. Hydrological Processes, 33(9), pp. 1292-1303.

Geyer, T., Birk, S., Reimann, T., Dorfliger, N., Sauter, M., 2013. Differentiated characterization of karst aquifers: Some contributions. Carbonates and Evaporites 28, 41–46. https://doi.org/10.1007/s13146-013-0150-9

Ghasemizadeh, R., Yu, X., Butscher, C., Padilla, I.Y., Alshawabkeh, A., 2016. Improved regional groundwater flow modeling using drainage features: a case study of the central northern karst aquifer system of Puerto Rico (USA). Hydrogeol. J. 24, 1463–1478. https://doi.org/10.1007/s10040-016-1419-6

Goldscheider, N., 2005. Karst groundwater vulnerability mapping: application of a new method in the Swabian Alb, Germany. Hydrogeology Journal. 13(4). pp. 555-564.

Gouzie, D., Berglund, J., Mickus, K.L., 2015. The application of quantitative fluorescent dye tracing to evaluate karst hydrogeologic response to varying recharge conditions in an urban area. Environ. Earth Sci. 74, 3099–3111. https://doi.org/10.1007/s12665-015-4348-0

Hartmann, A., 2016. Putting the cat in the box: why our models should consider subsurface heterogeneity at all scales. Wiley Interdiscip. Rev. Water 3, 478–486. https://doi.org/10.1002/wat2.1146

Hartmann, A., Antonio Barberá, J., Andreo, B., 2017. On the value of water quality data and informative flow states in karst modelling. Hydrol. Earth Syst. Sci. 21, 5971–5985. https://doi.org/10.5194/hess-21-5971-2017

Hartmann, A., Goldscheider, N., Wagener, T., Lange, J., Weiler, M., 2014. Karst water resources in a changing world: Approaches, of hydrological modeling. Rev. Geophys. 1–25. https://doi.org/10.1002/2013RG000443.Received

Hartmann, A., Mudarra, M., Andreo, B., Marin, A., Wagener, T., Lange, J., 2014. Modelling spatiotemporal impacts of hydroclimatic extremeson groundwater recharge at a Mediterranean karst aquifer. Water Resour. Res. 50, 6507–6521. https://doi.org/10.1002/2014WR015685.Received

Hull, L.C., 1980. Mechanisms controlling the inorganic and isotopic geochemistry of springs in a carbonate terrane. The Pennsylvania State University.

Kaufmann, G. and Braun, J., 1999. Karst aquifer evolution in fractured rocks. *Water resources research*, *35*(11), pp.3223-3238.

Kaufmann, G. and Braun, J., 2000. Karst aquifer evolution in fractured, porous rocks. *Water resources research*, *36*(6), pp.1381-1391.

Kavouri, K., Karatzas, G.P., 2015. Spatially Distributed Recharge in Karst Groundwater Modeling. 9th world Congr. EWRA.

Lauber, U., Ufrecht, W. and N. Goldscheider, N., 2014. Spatially resolved information on karst conduit flow from in-cave dye tracing. Hydrology and Earth System Sciences, 18(2), pp. 435-445.

Li, Z., Xu, X., Yu, B., Xu, C., Liu, M., Wang, K., 2016. Quantifying the impacts of climate and human activities on water and sediment discharge in a karst region of southwest China. J. Hydrol. 542, 836–849. https://doi.org/10.1016/j.jhydrol.2016.09.049

Luhmann, A.J., Covington, M.D., Alexander, S.C., Chai, S.Y., Schwartz, B.F., Groten, J.T., Alexander, E.C., 2012. Comparing conservative and nonconservative tracers in karst and

using them to estimate flow path geometry. J. Hydrol. 448–449, 201–211. https://doi.org/10.1016/j.jhydrol.2012.04.044
Luhmann, A.J., Covington, M.D., Myre, J.M., Perne, M., Jones, S.W., Alexander, E.C., Saar, M.O., 2015. Thermal damping and retardation in karst conduits. Hydrol. Earth Syst. Sci. 19, 137–157. https://doi.org/10.5194/hess-19-137-2015
Luhmann, A.J., Covington, M.D., Peters, A.J., Alexander, S.C., Anger, C.T., Green, J.A., Runkel, A.C., Alexander, E.C., 2011. Classification of Thermal Patterns at Karst Springs and Cave Streams. Ground Water 49, 324–335. https://doi.org/10.1111/j.1745-6584.2010.00737.x
Martin, J.B., Dean, R.W., 2001. Exchange of water between conduits and matrix in the Floridan aquifer.
Mckay, M.D., Beckman, R.J., Conover, W.J., 1979. A Comparison of Three Methods for selecting Input Variables in the Analysis of Output from a Computer code. Technometrics 21, 239–245. https://doi.org/10.1080/00401706.2000.10485979
Palmer, A.N., 1991. Origin and morphology of limestone caves. *Geological Society of America Bulletin*, *103*(1), pp.1-21.
Palmer, A.N., 1999. Patterns of dissolution porosity in carbonate rocks. Karst Model. Karst Waters Inst. Spec. Publ. 5 71–78.
Palmer, A.N., 1991. Origin and morphology of limestone caves. *Geological Society of America Bulletin*, *103*(1), pp.1-21.
Ronayne, M.J., 2013. Influence of conduit network geometry on solute transport in karst aquifers with a permeable matrix. Adv. Water Resour. 56, 27–34.
Siemers, J. and Dreybrodt, W., 1998. Early development of karst aquifers on percolation networks of fractures in limestone. *Water resources research*, *34*(3), pp.409-419.
Shoemaker, W.B., Kuniansky, E.L., Birk, S., Bauer, S., Swain, E.D., 2008. Documentation of a conduit flow process (CFP) for MODFLOW-2005.
Shuster, E.T., White, W.B., 1971. Seasonal fluctuations in the chemistry of lime-stone springs: A possible means for characterizing carbonate aquifers. J. Hydrol. 14, 93–128. https://doi.org/10.1016/0022-1694(71)90001-1
Taylor, C.J., Greene, E.A., 2008. Hydrogeologic characterization and methods used in the investigation of karst hydrology.
Toran, L., Herman, E.K., Berglund, J.L., 2019. Advances in Monitoring to Understand Flow Paths in Karst: Comparison of Historic and Recent Data from the Valley and Ridge of Pennsylvania, in: The Handbook of Environmental Chemistry. Springer, pp. 65–89.
Toran, L., Reisch, C.E., 2013. Using stormwater hysteresis to characterize karst spring discharge. Groundwater 51, 575–587. https://doi.org/10.1111/j.1745-6584.2012.00984.x
Waples, D.W. and Waples, J.S., 2004. A review and evaluation of specific heat capacities of rocks, minerals, and subsurface fluids. Part 1: Minerals and nonporous rocks. Natural resources research, 13(2), pp.97-122.
White, W.B., 1969. Conceptual models for carbonate aquifers. Groundwater 7, 15–21.
Xu, Z., Massei, N., Padilla, I., Hartmann, A., Hu, B., 2018. Characterization, modeling, and remediation of karst in a changing environment. Environ. Earth Sci. 77, 1–6. https://doi.org/10.1007/s12665-018-7660-7

Supporting Information

Please note: "Supporting Information" is generally *not* peer reviewed. Wiley is not responsible for the content or functionality of any supporting information supplied by the authors. Any queries (other than missing materials) should be directed to the corresponding author.

Table of contents for Supporting Information

Section 1: FEFLOW Governing Equations and Parameter List

Matrix equations

$$Q_\rho = S\frac{\partial h}{\partial t} - \nabla \cdot (K f_\mu B \cdot (\nabla h + \Theta e)) \quad (1)$$

$$Q_c = S\frac{\partial C}{\partial t} + q \cdot \nabla C - \nabla \cdot (B\varepsilon D \cdot \nabla C) + \Phi \mathrm{C} \quad (2)$$

$$Q_T = S\frac{\partial T}{\partial t} + q \cdot \nabla T - \nabla \cdot (B\Lambda \cdot \nabla T) + \Phi(\mathrm{T} - \mathrm{T}_o) \quad (3)$$

Fluid flux (Q_ρ)
Mass flux (Q_c)
Heat flux (Q_T)
Hydraulic head (h)
Specific storage (S)
Hydraulic conductivity (K)
Viscosity relation function (f_μ)
Buoyancy ratio (B)
Density ratio or buoyancy coefficient (Θ)
Gravitational unit vector (e)
Darcy flux (q)
Solute concentration (C)
Porosity (ε)
Molecular diffusion (D)
Transfer coefficient for mass or heat (Φ)

For mass, $\Phi = \pi R^2\left(\varepsilon \bar{Q}_\rho + \Re\vartheta\right)$

For heat, $\Phi = \pi R^2 \varepsilon \rho^f c^f \bar{Q}_\rho$

With addition terms defined in the conduit parameters

Temperature (T, T_o)
Thermal dispersion (Λ)

1-Dimensional Phreatic Darcy Feature Governing Equations and Parameters (used for conduits)

Heat flow through both liquid and solid necessities two equations for heat transport (Equations 6 and 7) which include heat flow through fluid ($\bar{Q}^f_T$) and solid ($\bar{Q}^s_\mathrm{T}$).

$$\bar{Q}_\rho = \frac{S\frac{\partial h}{\partial t} - \nabla\cdot\left(K f_\mu B \cdot (\nabla h + \Theta e)\right)}{\pi R^2 \varepsilon} \quad (4)$$

$$\bar{Q}_c = \frac{S\frac{\partial C}{\partial t} + \pi R^2 \varepsilon v \cdot \nabla C - \nabla \cdot \left(\left(\pi R^2 \varepsilon (D_d I + D_m) \cdot \nabla C \right) + \pi R^2 \left(\varepsilon \bar{Q}_\rho + \Re \vartheta \right) \mathrm{C} \right.}{\pi R^2 \varepsilon} \tag{5}$$

$$\bar{Q}_T = \frac{S\frac{\partial T}{\partial t} + \pi R^2 \varepsilon \rho^f c^f v \cdot \nabla T - \nabla \cdot \left(\pi R^2 \{ [\varepsilon \lambda^f + (1-\varepsilon)\lambda^s] I + \varepsilon \rho^f c^f D_m \} \cdot \nabla T \right) + \pi R^2 \varepsilon \rho^f c^f \bar{Q}_\rho (\mathrm{T} - \mathrm{T}_o)}{\pi R^2} \tag{6}$$

and

$$\bar{Q}_T = \varepsilon \rho^f \bar{Q}_T^f + (1-\varepsilon)\rho^s \bar{Q}_T^s \tag{7}$$

Fluid flux ($\bar{Q}_\rho$)
Chemical decay rate (ϑ)
Mass flux ($\bar{Q}_c$)
Heat flux ($\bar{Q}_T$)
Conduit radius (R)
Velocity vector of fluid (v)
Molecular diffusion coefficient (D_d)
Mechanical dispersion tensor (D_m)
Solute retardation ($\Re$)
Thermal conductivity of fluid (λ^f)
Thermal conductivity of solid (λ^s)
Specific heat capacity of fluid (c^f)
Density of fluid (ρ^f)
Density of solid (ρ^s)

For a more complete description of the above equations refer to Diersch (2009).

Section 2: Field set up, model parameters, and additional details on results

Figure S1. Steady-state dye mixture injected into Tippery Sink

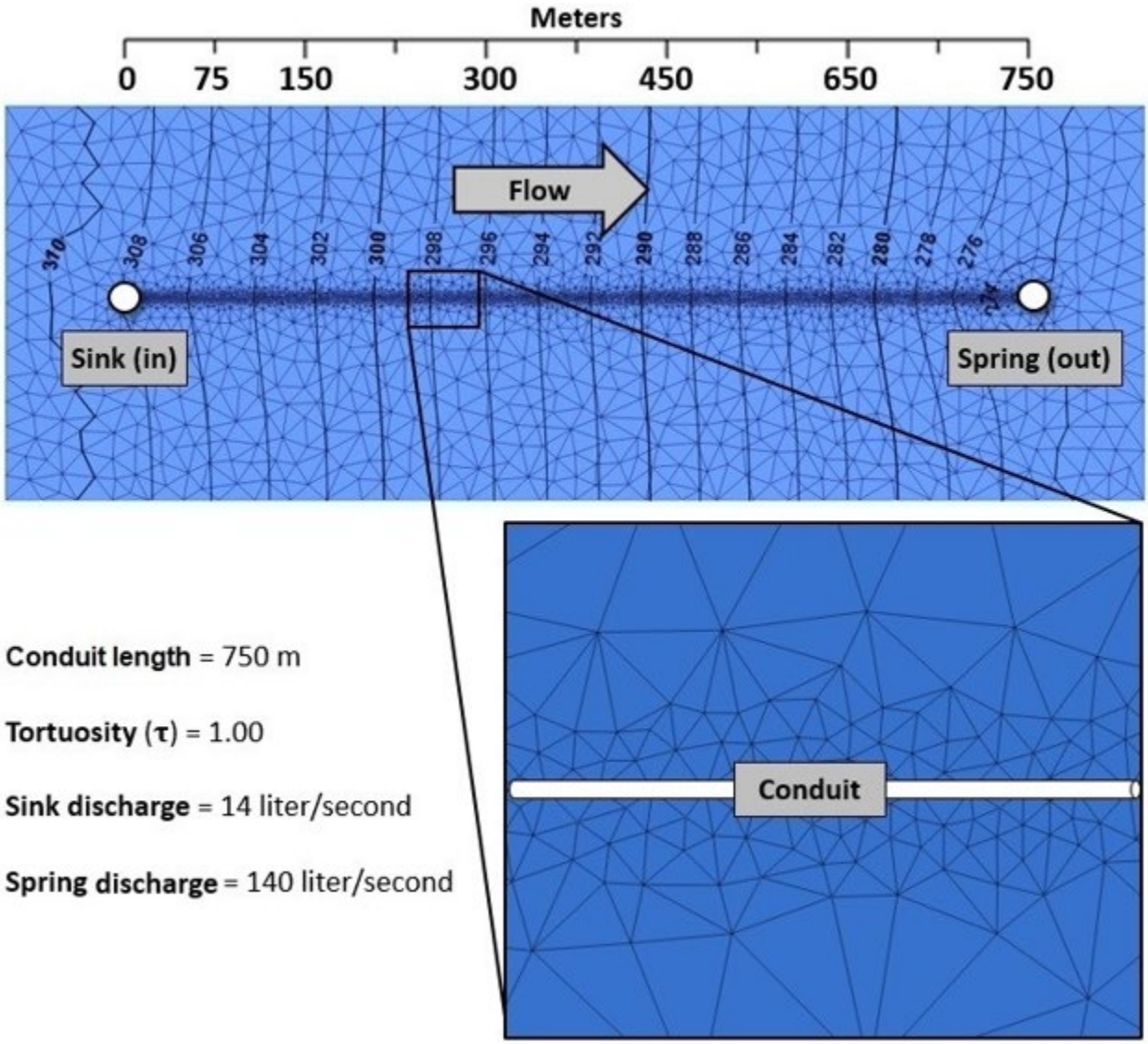

Figure S2. Example FEFLOW model grid setup for a single straight conduit. Contours indicate steady state head elevation in meters above sea level.

Table S1. Latin Hypercube sensitivity analysis model runs

Model Run ID		Model Parameters					Model Breakthrough Curve Results					
		Conduit K (m/s)	Conduit Area (m^2)	Matrix Transm. (m^2/s)	Porosity (n)	Dispersivity Modifier	16% Dye Arrival (days)	50% Dye Arrival (days)	84% Dye Arrival (days)	Peak Arrival (days)	Dye Curve Width (days)	Peak Height Ratio (model/obs)
Geometry 1 (straight conduit)	Base	0.105	0.50	0.00050	0.10	1.00	2.10	2.46	3.14	2.31	1.03	1.37
	LHC1	0.075	0.92	0.00032	0.15	1.15	2.73	3.14	3.68	3.01	0.95	1.31
	LHC8	0.156	0.60	0.00101	0.13	0.08	1.46	1.69	2.01	1.63	0.55	4.47
	LHC9	0.101	0.44	0.00033	0.13	1.32	2.16	2.51	3.09	2.36	0.94	1.70
	LHC11	0.087	0.67	0.00107	0.14	0.29	2.50	2.90	3.51	2.75	1.01	1.79
	LHC14	0.010	0.55	0.00016	0.04	1.04	-	-	-	-	-	-
	LHC16	0.124	0.78	0.00067	0.06	2.41	1.74	2.04	2.66	1.92	0.92	1.61
	LHC20	0.114	0.21	0.00001	0.04	1.14	0.71	0.86	1.02	0.86	0.31	3.32
	LHC25	0.140	0.25	0.00013	0.01	1.25	1.19	1.36	1.55	1.35	0.36	2.51
	LHC32	0.170	0.42	0.00017	0.11	0.87	1.30	1.52	1.76	1.48	0.46	2.91
	LHC35	0.060	0.40	0.00020	0.01	0.77	1.88	2.47	2.91	2.60	1.03	0.87
	LHC37	0.025	0.66	0.00059	0.14	1.07	-	-	-	9.61	-	0.13
	LHC39	0.042	0.51	0.00114	0.11	1.01	-	-	-	6.11	-	0.22
	LHC50	0.198	0.30	0.00035	0.10	1.44	1.30	1.56	2.04	1.46	0.74	1.80
Geometry 2 (forked conduit)	Base	0.105	0.50	0.00050	0.10	1.00	1.33	1.60	2.14	1.48	0.80	1.04
	LHC10	0.177	1.06	0.00014	0.17	2.09	0.61	0.80	1.34	0.77	0.73	3.09
	LHC12	0.159	0.33	0.00026	0.20	1.68	0.96	1.27	2.75	1.05	1.79	1.00
	LHC13	0.009	0.89	0.00003	0.07	0.65	-	-	-	-	-	-
	LHC19	0.129	0.49	0.00050	0.02	0.49	0.95	1.14	1.34	1.10	0.40	2.31
	LHC22	0.117	0.26	0.00065	0.07	0.68	1.46	1.79	2.48	1.60	1.02	0.57
	LHC26	0.064	0.55	0.00046	0.12	1.85	0.78	1.17	2.09	0.86	1.31	0.35

Table S1 (continued)

Model Run ID		Model Parameters					Model Breakthrough Curve Results					
		Conduit K (m/s)	Conduit Area (m^2)	Matrix Transm. (m^2/s)	Porosity (n)	Dispersivity Modifier	16% Dye Arrival (days)	50% Dye Arrival (days)	84% Dye Arrival (days)	Peak Arrival (days)	Dye Curve Width (days)	Peak Height Ratio (model/obs)
Geometry 2 (forked)	LHC27	0.090	0.20	0.00040	0.15	1.20	2.46	3.30	5.04	2.64	2.58	0.09
	LHC31	0.210	0.34	0.00048	0.05	1.51	0.70	0.89	1.17	0.85	0.47	1.71
	LHC40	0.035	0.52	0.00061	0.18	0.26	4.60	5.47	7.23	5.00	2.62	0.23
	LHC41	0.049	0.57	0.00090	0.16	0.54	3.49	4.22	5.59	3.79	2.10	0.21
	LHC43	0.141	0.27	0.00022	0.09	0.20	0.79	0.95	1.09	0.95	0.30	3.02
	LHC44	0.104	0.47	0.00071	0.08	0.91	1.49	1.78	2.34	1.65	0.85	0.84
	LHC46	0.080	0.82	0.00055	0.18	0.35	1.67	1.94	2.43	1.84	0.76	1.68
Geometry 3 (tortuous conduit)	Base	0.105	0.50	0.00050	0.10	1.00	2.14	2.44	2.83	2.36	0.70	1.52
	LHC2	0.039	0.74	0.00051	0.06	1.35	-	-	-	5.32	-	0.41
	LHC4	0.182	0.02	0.00037	0.03	0.74	-	-	-	-	-	0.32
	LHC5	0.066	0.53	0.00084	0.05	1.39	1.66	4.57	7.47	3.34	5.81	0.51
	LHC15	0.119	0.12	0.00045	0.10	1.92	-	-	-	4.00	-	0.09
	LHC18	0.107	0.80	0.00043	0.10	1.95	2.10	2.45	3.19	2.29	1.08	1.66
	LHC24	0.163	0.70	0.00053	0.07	0.03	1.36	1.55	1.74	1.54	0.38	5.54
	LHC29	0.082	0.16	0.00094	0.25	1.77	-	-	-	-	-	-
	LHC36	0.020	0.75	0.00054	0.21	0.71	-	-	-	11.68	-	0.08
	LHC45	0.220	0.38	0.00028	0.12	1.11	1.24	1.44	1.66	1.41	0.42	3.22
	LHC48	0.132	0.36	0.00088	0.05	1.58	1.82	2.51	5.94	1.91	4.11	0.97
	LHC49	0.094	0.29	0.00056	0.09	1.22	2.72	3.45	8.28	2.86	5.56	0.47
	LHC51	0.147	0.47	0.00070	0.03	1.00	1.41	1.63	1.86	1.58	0.46	2.50
	LHC52	0.051	0.86	0.00004	0.03	0.94	2.67	3.01	3.40	2.96	0.73	1.85

Table S1 (continued)

Model Run ID		Model Parameters					Model Breakthrough Curve Results					
		Conduit K (m/s)	Conduit Area (m^2)	Matrix Transm. (m^2/s)	Porosity (n)	Dispersivity Modifier	16% Dye Arrival (days)	50% Dye Arrival (days)	84% Dye Arrival (days)	Peak Arrival (days)	Dye Curve Width (days)	Peak Height Ratio (model/obs)
Geometry 4 (anastomosing conduits)	Base	0.105	0.50	0.00050	0.10	1.00	2.70	3.57	7.04	2.80	4.34	0.92
	LHC3	0.166	0.63	0.00082	0.09	1.55	1.82	2.30	3.81	1.93	1.99	1.15
	LHC6	0.086	0.58	0.00067	0.01	0.17	2.53	2.83	3.16	2.80	0.63	2.90
	LHC7	0.121	0.15	0.00079	0.11	0.54	-	-	-	6.72	-	0.20
	LHC17	0.189	0.62	0.00026	0.13	0.45	-	-	-	-	-	-
	LHC21	0.055	0.64	0.00058	0.15	1.44	5.22	7.23	10.29	-	5.07	-
	LHC23	0.149	0.15	0.00073	0.16	0.56	-	-	-	2.76	-	0.16
	LHC28	0.021	0.37	0.00074	0.10	0.85	-	-	-	-	-	-
	LHC30	0.108	0.04	0.00077	0.08	1.65	-	-	-	-	-	0.10
	LHC33	0.039	0.45	0.00042	0.06	0.80	-	-	-	7.10	-	0.28
	LHC34	0.243	0.71	0.00008	0.12	1.30	-	-	-	-	-	-
	LHC38	0.098	0.98	0.00039	0.19	0.60	5.52	6.90	9.44	5.99	3.92	0.05
	LHC42	0.134	0.68	0.00062	0.08	0.95	2.20	2.67	4.18	2.34	1.98	1.11
	LHC47	0.071	0.43	0.00034	0.12	0.40	3.74	0.36	9.39	3.95	5.65	0.85

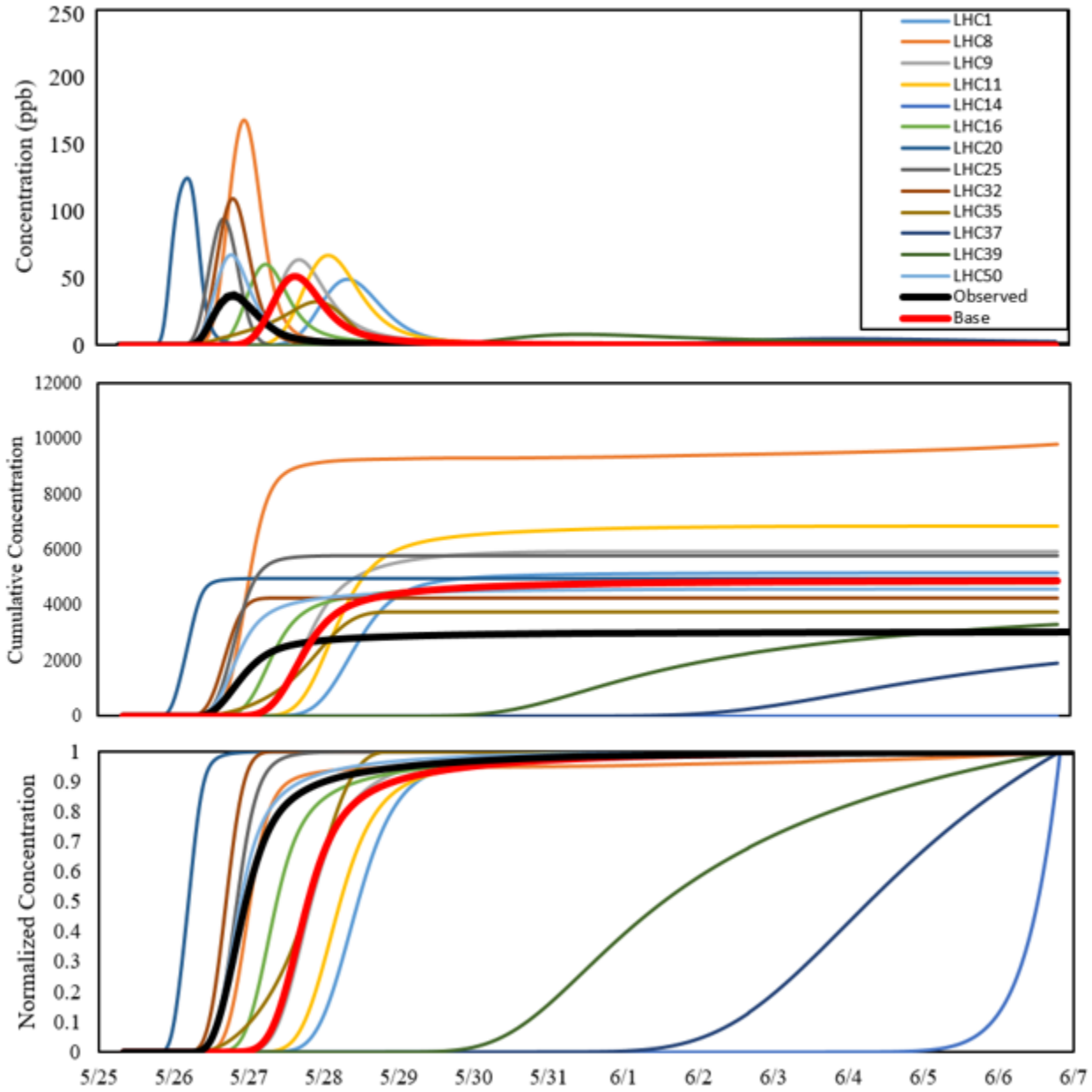

Figure S3. Geometry 1 breakthrough curve results.

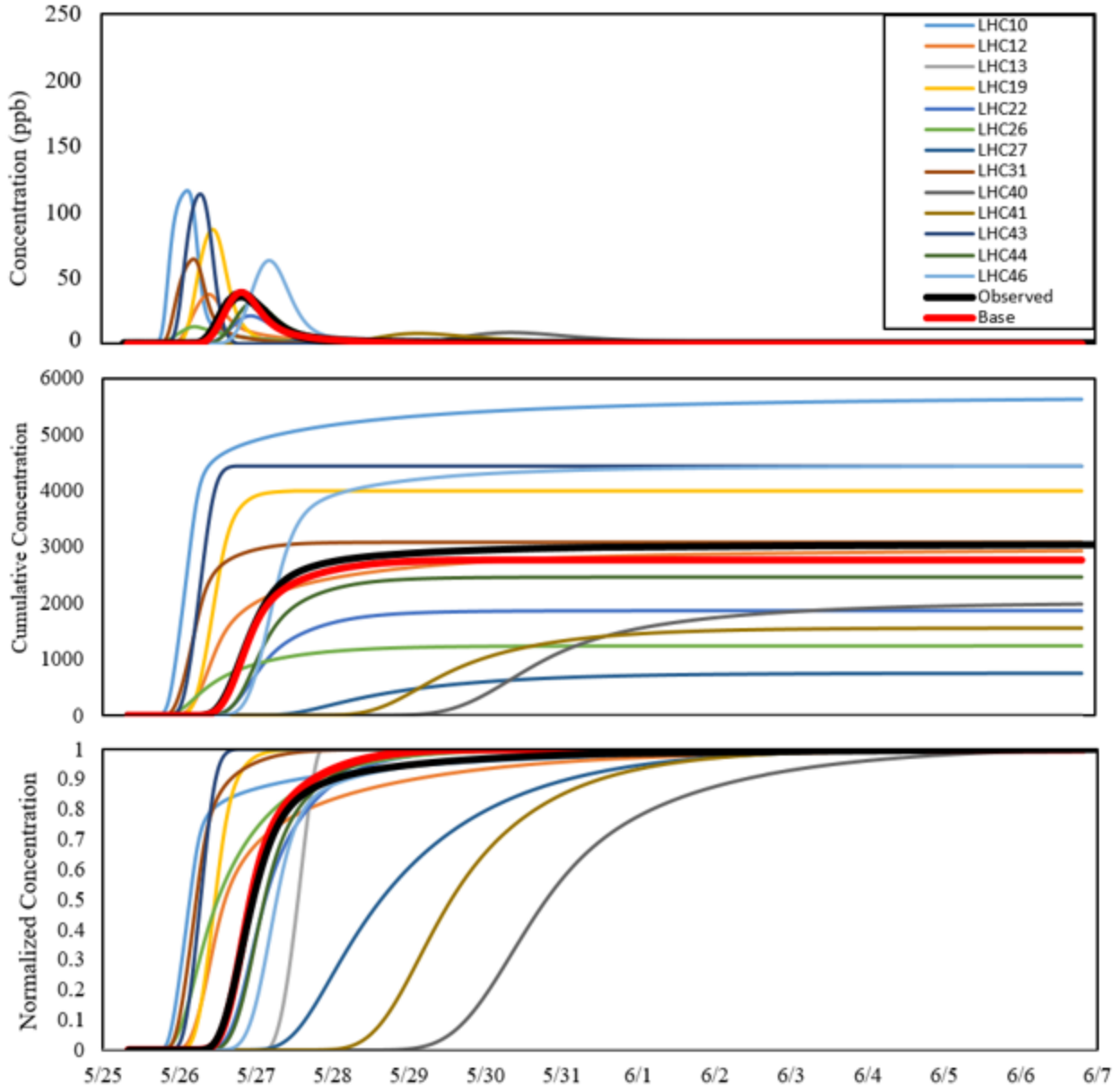

Figure S4. Geometry 2 breakthrough curve results.

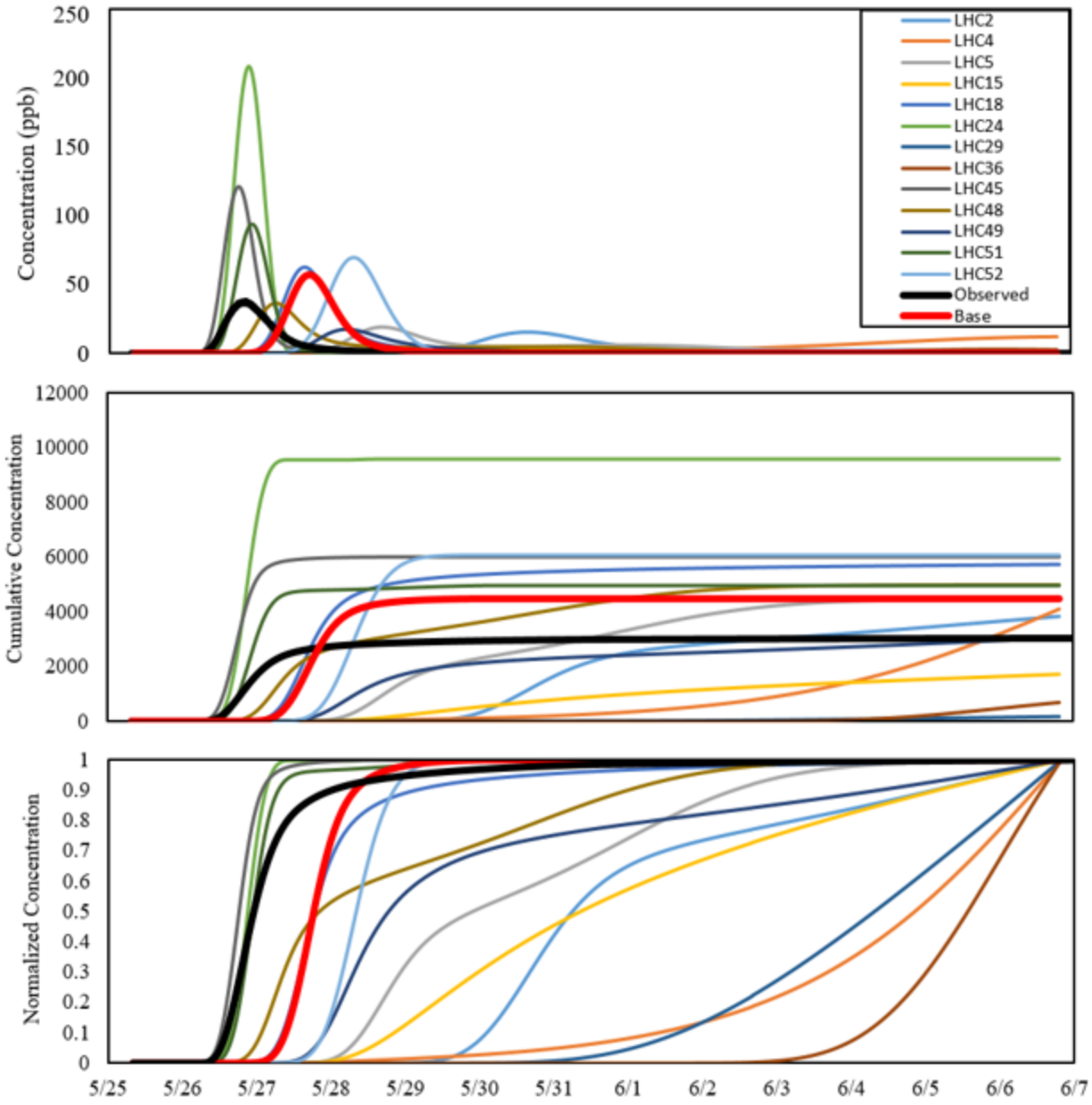

Figure S5. Geometry 3 breakthrough curve results.

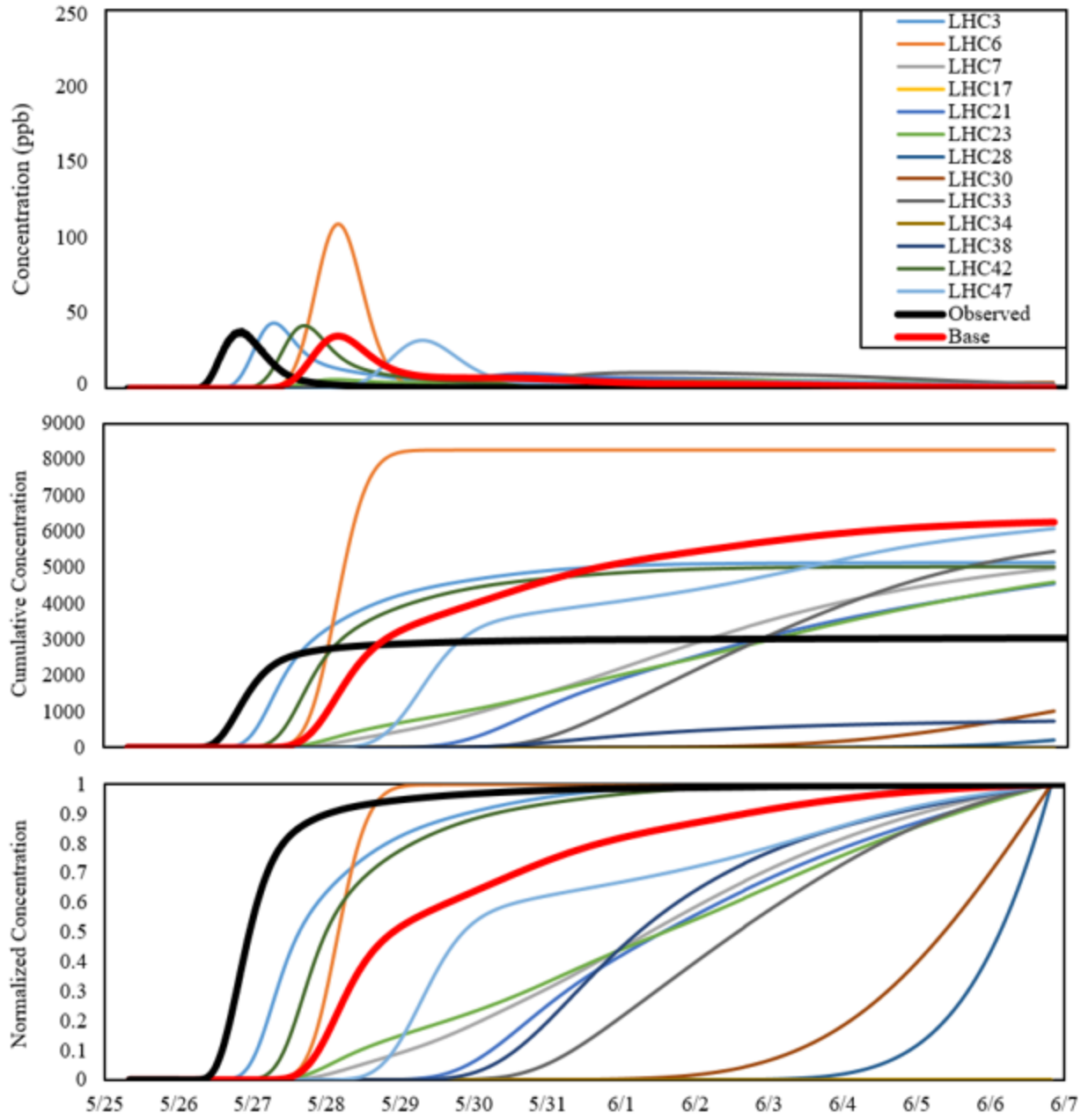

Figure S6. Geometry 4 breakthrough curve results.

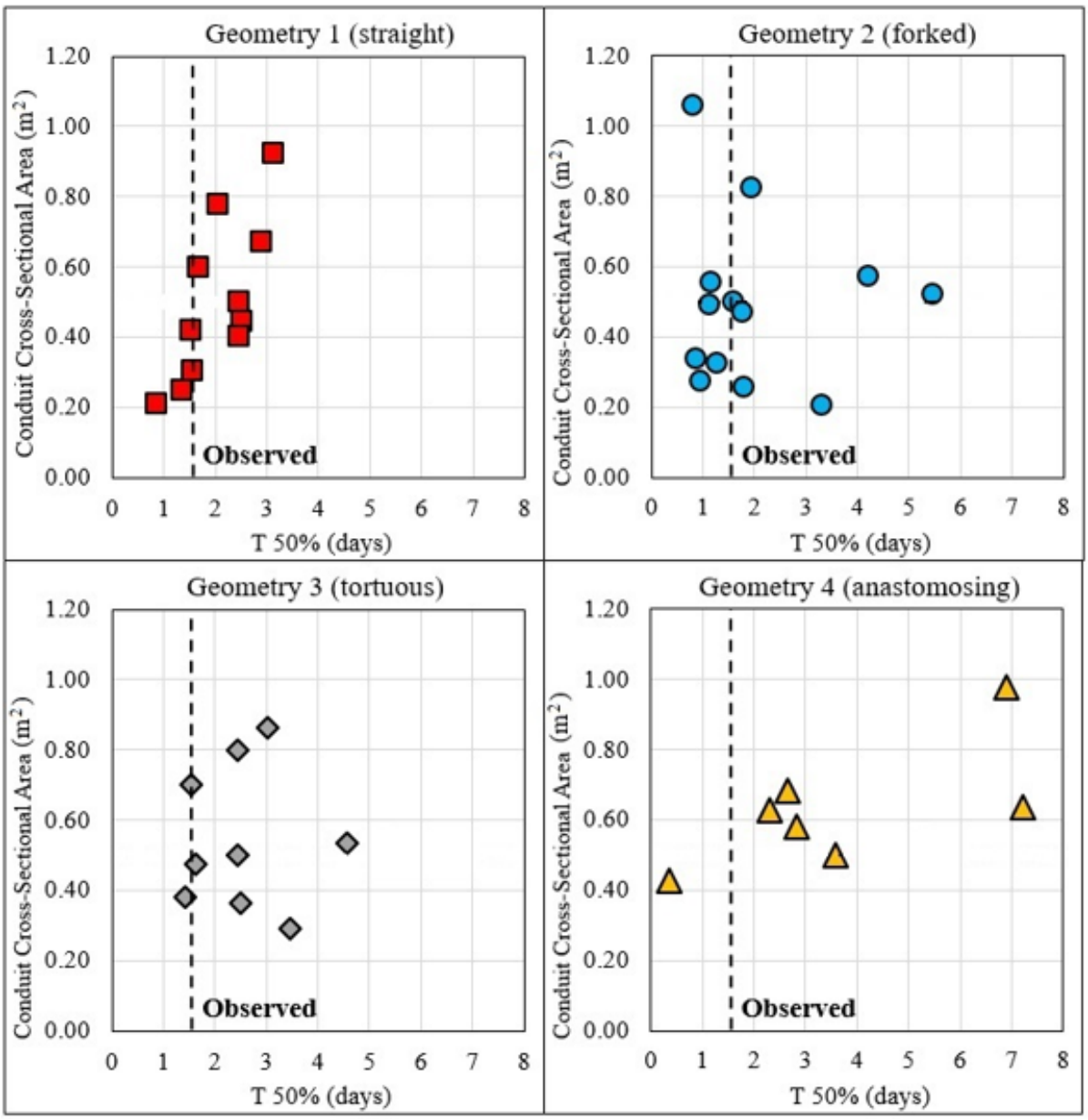

Figure S7. Modeled 50% dye arrival time vs. conduit cross-sectional area for Conduit Geometry 1-4 Scenarios.

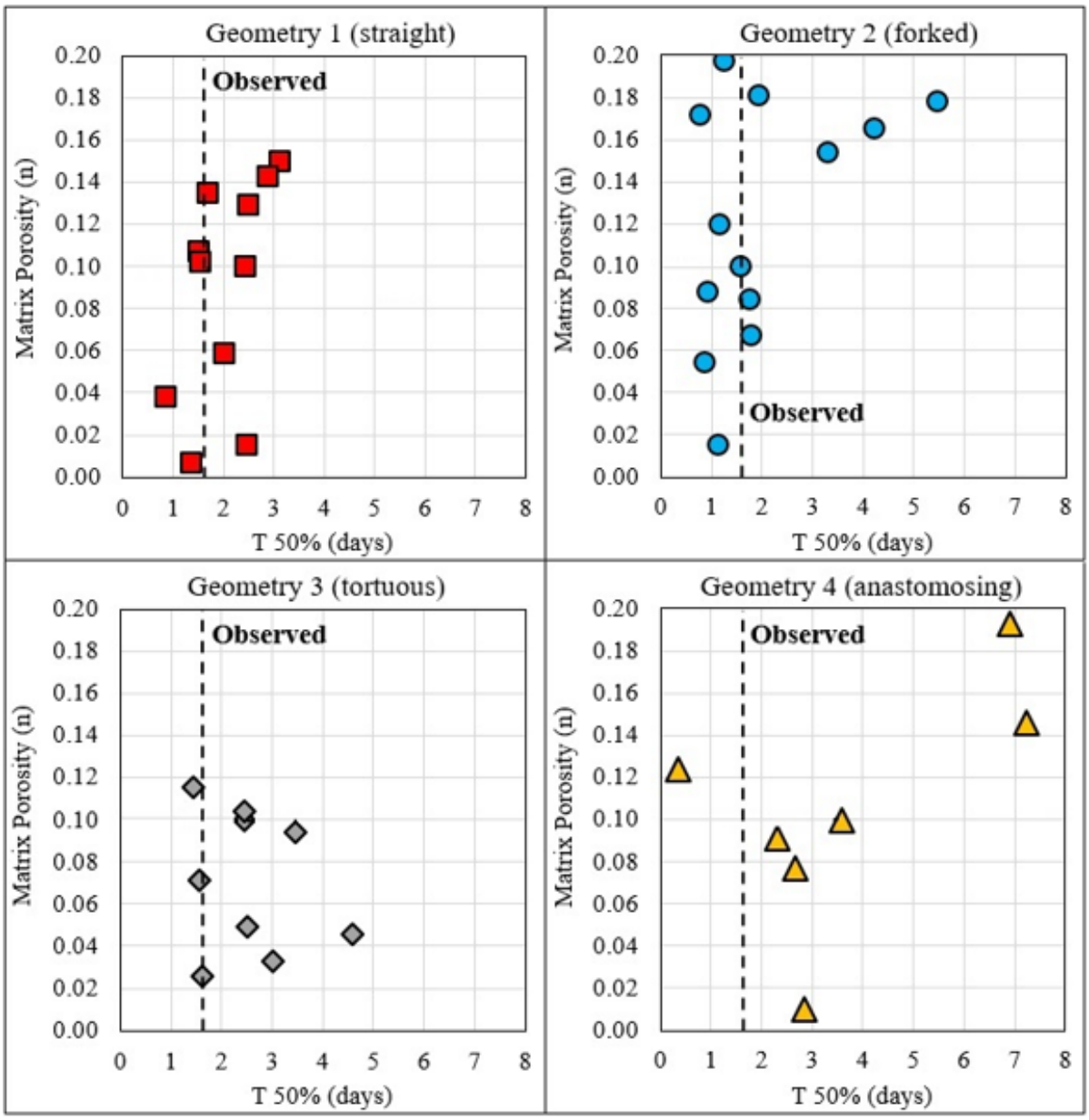

Figure S8. Modeled 50% dye arrival time vs. matrix porosity for Conduit Geometry 1-4 scenarios.

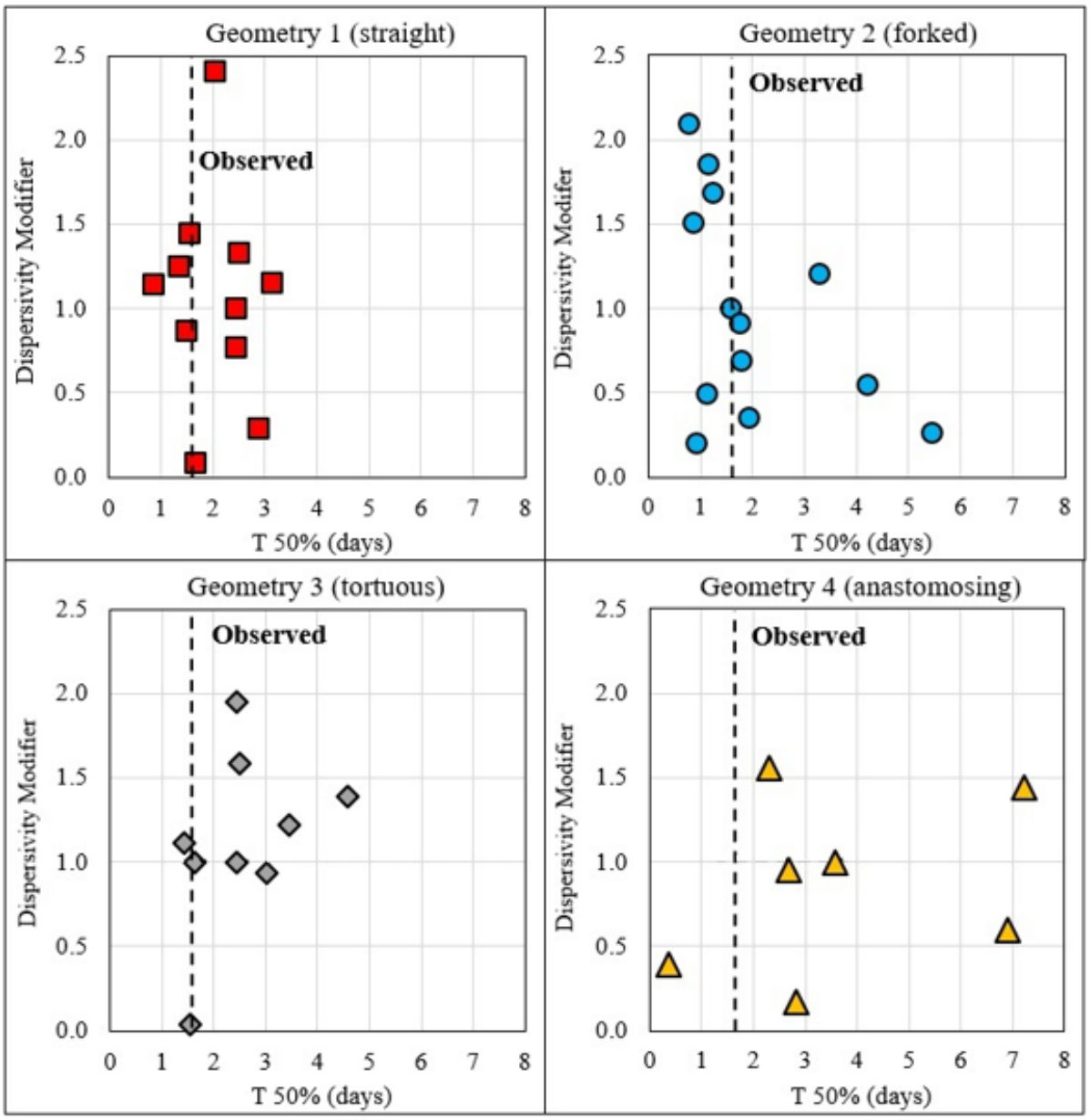

Figure S9. Modeled 50% dye arrival time vs. dispersivity modifier for Conduit Geometry 1-4 scenarios.

Section 3: Additional model runs

Additional model configurations for the forked conduit are presented in this section. The distance to the fork was evaluated in Figure S9. When the fork is closer to the spring (proximal), breakthrough occurs earlier and with a higher peak than observed. A model was also constructed with a semi-forked conduit – that is, only one side-branching conduit, dye is only pirated by flow to one side. Less flow was diverted, which results in a greater overall concentration of dye reaching the spring (Figure S10). Similar to the tortuous conduit, a large recession tail was created as the dye which would have been pirated away from a symmetrical conduit instead feeds back into the main conduit.

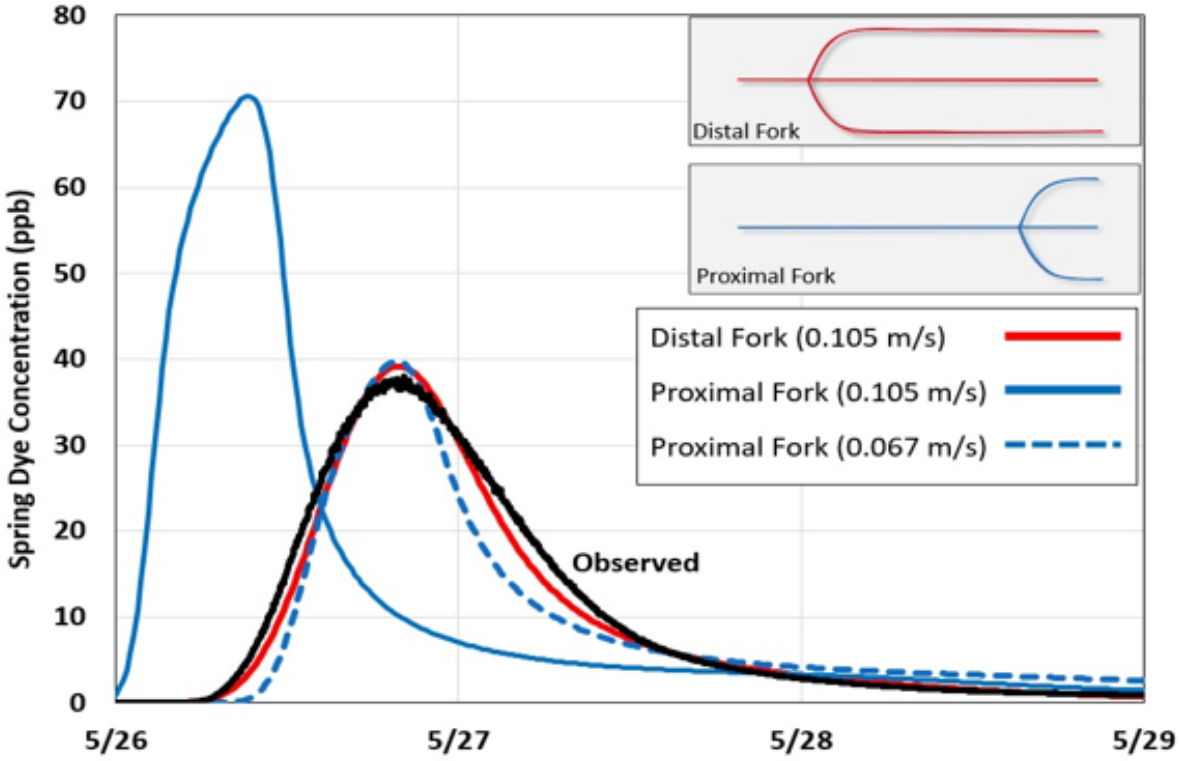

Figure S10. Decreased conduit conductivity comparison in the Proximal Fork model resulting in a delayed peak response to better match the observed dye concentrations.

The forked conduit model (Geometry 2) resulted in the best match with observed dye concentrations but also depended on the location of the fork. With all other parameters equal, a split occurring closer to the spring results in a faster dye arrival time and a greater peak concentration. This effect is likely the result of the steepened gradient within the main conduit resulting from shifting the conduit split (and therefore the effect of the split on the main conduit) closer to the spring. This resulting decrease in arrival time and increase in peak concentration can be somewhat offset by increasing the conduit conductivity, as seen in the example with the Proximal Fork model, but the resulting curve still does not provide as good a match as the Distal Fork model. Specifically, there is a notable decrease in dye concentrations in both the rising and falling limbs, and a more drawn-out dye recovery. This may be the result of greater matrix interaction in the conduit segment between the sink and the fork point due to the decreased conductivity contrast between the conduit and the matrix. This extra interaction between the

conduit and matrix would result in an initially decreased dye peak concentration followed by dye re-entering the conduit as the dye plume passes through the conduit, which appears to be supported by these findings. As such, not only does the moving of the branching point affect timing of the dye arrival, it will also have an effect on the rising and falling limbs, along with the recovery tail. These relationships further help constrain the conceptual model and flow behavior of the conduit connecting the sinking stream and spring.

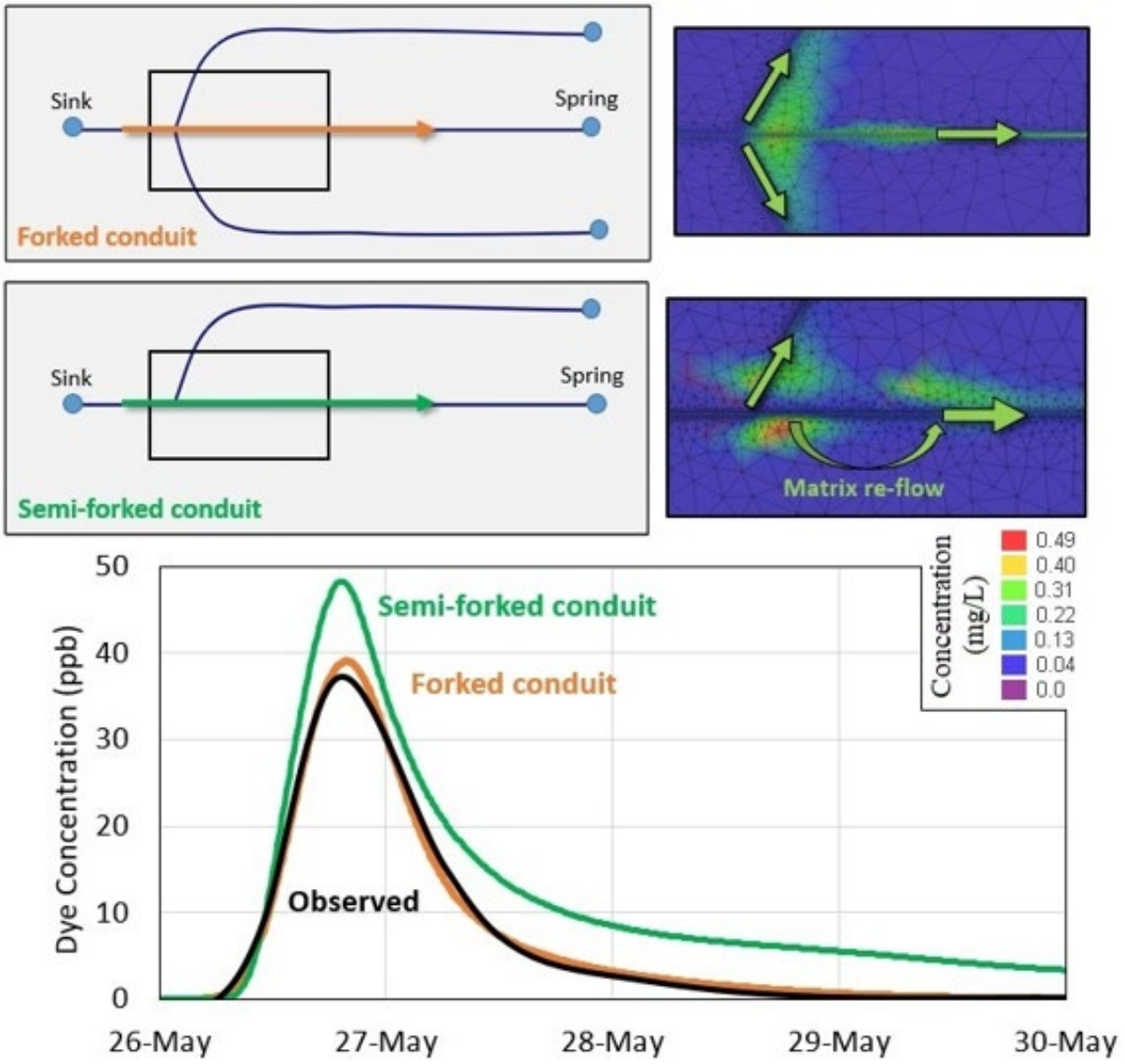

Figure S11. Effect of single and dual conduit branching on the modeled dye breakthrough curve.

To explore the possibility of the forked conduit model being convergent (side conduits feeding the main conduit) rather than divergent (side conduits flowing away from the main conduit) a reverse fork model was constructed and tested (Figure S12). While it was possible to accomplish a breakthrough peak time which closely matched both the observed and straight conduit model, it was not able to adequately reproduce peak dye concentration or the sharpness of the dye recession tail.

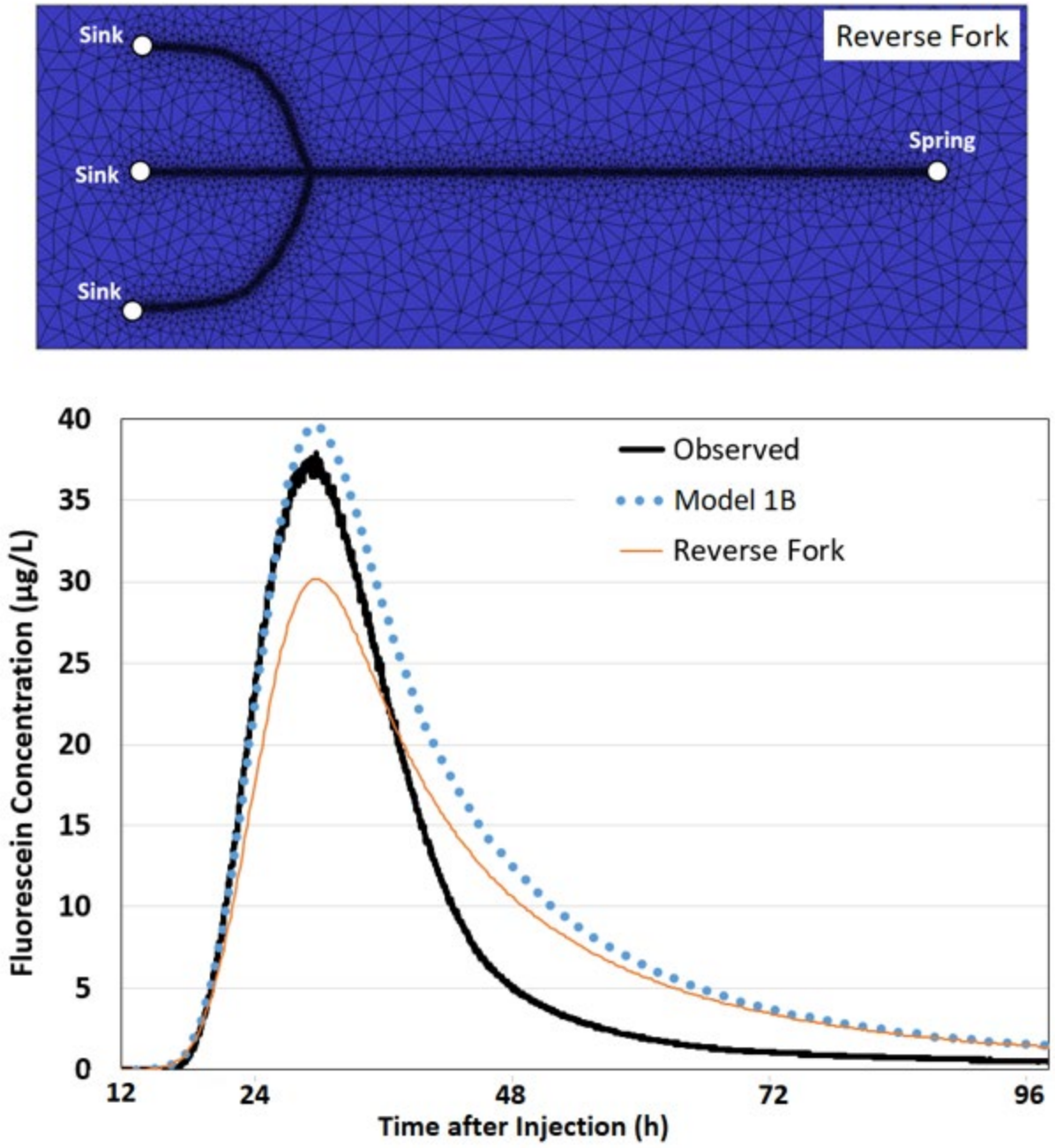

Figure S12. Comparison of reverse fork and straight conduit model dye trace breakthrough curves.

To test the effect of varied the varied recharge value within the 1000 m x 300 m model domain, two additional models were ran and analyzed for Model 2 (the forked conduit geometry) at 1-meter per year, 0.5-meter per year, and 0.33 meter per year recharge. Due to the relatively small area of the model domain relative to the calculated capture area for the sinking stream there was little difference between the modeled dye breakthrough curves (Figure S13).

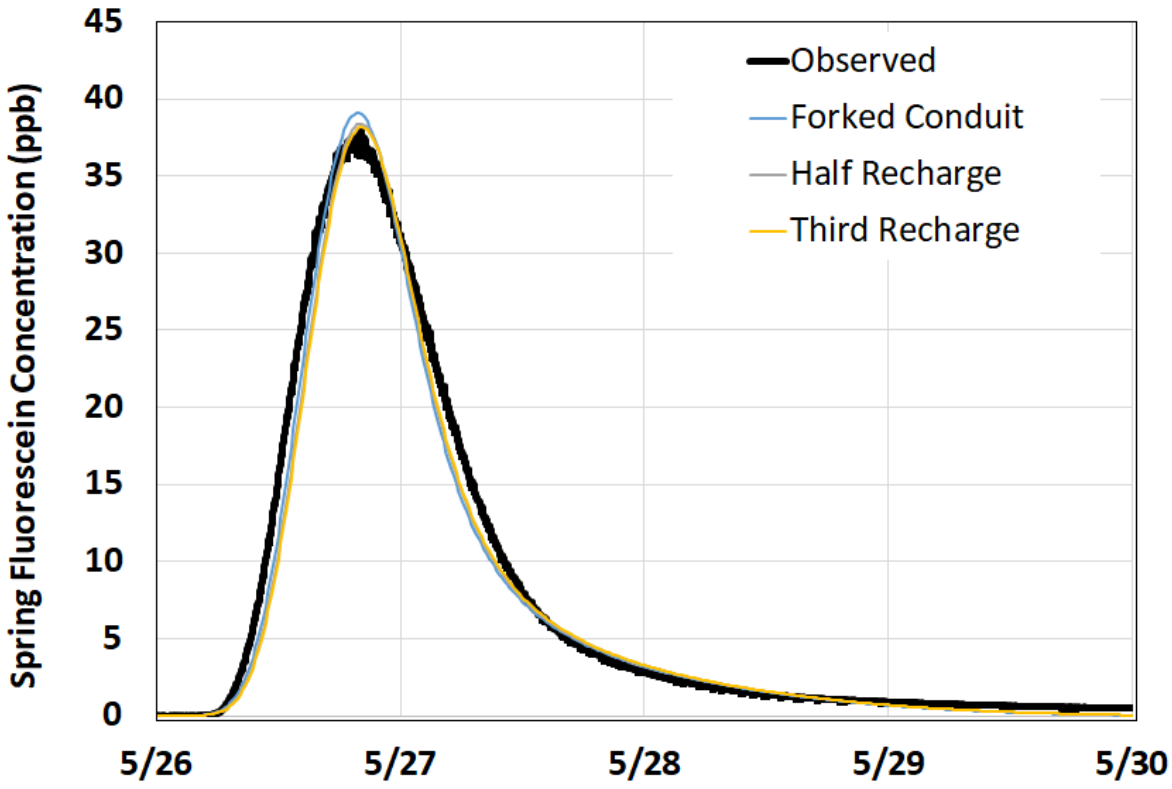

Figure S13. Comparison of modeled dye concentration breakthrough curves at 1-meter, 0.5-meter, and 0.33 meter per year recharge within the model domain.